



저작자표시-비영리-변경금지 2.0 대한민국

이용자는 아래의 조건을 따르는 경우에 한하여 자유롭게

- 이 저작물을 복제, 배포, 전송, 전시, 공연 및 방송할 수 있습니다.

다음과 같은 조건을 따라야 합니다:



저작자표시. 귀하는 원저작자를 표시하여야 합니다.



비영리. 귀하는 이 저작물을 영리 목적으로 이용할 수 없습니다.



변경금지. 귀하는 이 저작물을 개작, 변형 또는 가공할 수 없습니다.

- 귀하는, 이 저작물의 재이용이나 배포의 경우, 이 저작물에 적용된 이용허락조건을 명확하게 나타내어야 합니다.
- 저작권자로부터 별도의 허가를 받으면 이러한 조건들은 적용되지 않습니다.

저작권법에 따른 이용자의 권리는 위의 내용에 의하여 영향을 받지 않습니다.

이것은 [이용허락규약\(Legal Code\)](#)을 이해하기 쉽게 요약한 것입니다.

[Disclaimer](#)

공학박사 학위논문

**Fabrication of Thin Film Encapsulation
(TFE) by ICP-CVD & Roll to Roll
Reactive Magnetron Sputtering for
OLED Display**

유도결합플라즈마 & 롤투롤 마그네트론
스퍼터링을 이용한 OLED 디스플레이용
박막봉지 제작

2020 년 2 월

서울대학교 대학원
재료공학부
방 성 환

Fabrication of Thin Film Encapsulation (TFE) by ICP-CVD & Roll to Roll Reactive Magnetron Sputtering for OLED Display

Advisor: Prof. Nong-Moon Hwang

By

Sunghwan Bang

**A dissertation submitted to the Graduated Faculty of Seoul
National University in partial fulfillment of the requirements
for the Degree of Doctor of Philosophy
Department of Materials Science and Engineering**

February 2020

Approved

By

Chair
Vice Chair
Examiner
Examiner
Examiner

Yongsok Seo	(Seal)
Nong-Moon Hwang	(Seal)
Ho Won Jang	(Seal)
Woo Hee Kim	(Seal)
In Chan Hwang	(Seal)

Abstract

Fabrication of Thin Film Encapsulation (TFE) by ICP-CVD & Roll to Roll Reactive Magnetron Sputtering for OLED Display

Sunghwan Bang

Department of Materials Science and Engineering

The Graduate School

Seoul National University

The flexible organic light emitting diode display has recently attracted great attention in the display market because it has superior characteristics such as color gamut, contrast ratio, viewing angle, and power consumption compared to a conventional liquid crystal display. In particular, unlike a liquid crystal display that emits light through a BLU (Back Light Unit), an organic light emitting diode has characteristics of self-emission and thus a device having a thin thickness can be

manufactured, which has a great advantage in terms of design freedom. Despite of having such excellent characteristics, the flexible organic light emitting diode display uses a polymer as a substrate when manufacturing a device, and unlike the liquid crystal display that used glass, oxygen or moisture in the air is permeated well into the substrate and thus, they react organic materials and aluminum electrodes, which causes problems such as oxidation, crystallization and peeling. This results in areas of black spots that are not illuminated. Therefore, in order to solve such a problem, an encapsulation film technology capable of blocking moisture from the outside has become important. In particular, in the field of foldable displays having a radius of curvature of 1.5 mm or less, development of a thin film encapsulation technology having excellent moisture permeation resistance has become very important. Thin-film encapsulation technology refers to a technique of depositing a water-permeable barrier on a flexible substrate such as a polymer substrate, and it has an advantage of manufacturing a thinner and lighter device than a conventional metal can/glass encapsulation method. However, the thin film encapsulation technology has a disadvantage in that the water permeation characteristics are inferior to conventional glass due to the thin film thickness and defects generated during deposition. In order to overcome this problem, ViTEX 株式会社 has proposed an organic / inorganic hybrid structure, which is formed by alternately stacking a high density inorganic film that prevents water permeation and an organic film that can secure flexibility. In other words, the defects were complemented with a multilayered film structures and the flexibility of the encapsulation film was ensured with the organic layer. Currently, manufacturers of flexible OLED displays are applying the organic / inorganic layers mentioned above alternately and applying them to the moisture barrier. However, each company has an

optimized organic / inorganic film type and structure, and has been actively researching materials and deposition technologies in terms of excellent water permeation prevention properties and high productivity. Inorganic thin film encapsulation technology can be deposited by chemical vapor deposition, atomic layer deposition, sputtering, etc. Among these techniques, inorganic film deposition using atomic layer deposition It shows the most excellent characteristic in this water permeation prevention property. However, the deposition rate is very low as 6-7nm / min is still difficult to apply to mass production technology. Therefore, in case of inorganic film deposition, research on encapsulation film technology using gas phase chemical vapor deposition is the most conducted at present. However, in the case of the PE-CVD method, since the process temperature must be deposited at 100°C or lower during the deposition of the encapsulation film, it is difficult to form a high quality encapsulation film having a high density of thin films with few defects at low temperatures. Recently, research on thin film encapsulation technology with high deposition rate and low moisture permeability at low temperature is being actively conducted through the development of various deposition equipment and methods.

At the first chapter of this study, we developed new SiO_xN_y thin film using ICP-CVD and presented new insights into the principle of formation of high quality moisture barrier film by non-classical CVD approach based on charged nanoparticle theory. In order to determine whether SiO_xN_y nanoparticles are produced in the gas phase according to various process variables, the nanoparticles generated in the gas phase were captured by using a TEM grid, and the captured SiO_xN_y nanoparticles were analyzed by TEM for the first time. Through TEM analysis, we confirmed that 20- 300

nm-sized SiO_xN_y nanoparticles were formed in the gas phase. In the observed nanoparticles, the size, shape, and degree of aggregation between nanoparticles were significantly different according to the process conditions. When the argon/silane ratio was low and the power was low, the nanoparticles formed in the gas phase were large in size, irregular in shape, and largely aggregated among the nanoparticles, and were also amorphous nanoparticles.

On the other hand, the higher the argon/silane ratio and the higher the power, the smaller the size of the nanoparticles and uniform nanoparticles were confirmed. In addition, the resulting nanoparticles had a circular shape and the aggregation between the nanoparticles gradually disappeared. Under optimized conditions, single and circular nanoparticles of 20-30nm size without any aggregation between nanoparticles were identified, and even single-crystal nanoparticles were identified under specific power conditions. After confirming the initial nanoparticle behavior generated in the gas phase through the TEM analysis, the actual moisture permeation resistance characteristics were confirmed through thin film deposition. The film deposited at high argon / silane ratio with high power has 1,000 times superior barrier property than the film deposited at low argon / silane ratio with low power. Through this study, we confirmed and suggested for the first time that there is a strong correlation between the behavior of SiO_xN_y nanoparticles generated in the gas phase and the formation of high density encapsulation film at low temperature of ~100 °C. It is expected that this non-classical CVD approach based on the theory of charged nanoparticles play a significant role controlling various thin film properties at various electronic field.

At the second chapters of this study, silicon oxide (SiO_x) barrier films were deposited on polyethylene terephthalate (PET) substrate at 20 °C using reactive dual magnetron sputtering system. The oxygen flow rate, input sputtering power and film thickness were changed to optimize the barrier properties of SiO_x films. Details of sputtering power and film thickness effects on the SiO_x properties in terms of residual stress, surface, roughness, density, interface of SiO_x/PET, and water vapor transmission rate (WVTR) were investigated. Especially, we focused our attention on the effects of sputtering power on the final barrier properties. A high density of 2.42 g/cm³ SiO_x film with high transmittance of 92% was obtained. Even at low substrate temperature of 20°C, the 300 nm-thick SiO_x barrier film exhibited superior WVTR value of 7.7×10^{-3} g/m²/day as a single barrier layer using roll to roll reactive sputtering.

Keyword : Flexible OLED display, Thin Film Encapsulation, ICP-CVD, Non-Classical CVD, Theory of Charged Nanoparticles, , SiO_xNy, SiO_x, Magnetron Sputtering

Contents

Abstract	i
Contents	vi
List of Figures	ix
List of Tables	xv
Chapter1. Introduction	1
1.1 Basic Principle and Structure of OLED Device.....	1
1.2 Issue of Flexible OLED Display.....	3
1.3 Encapsulation of OLED Display.....	5
1.4 Consideration of Formation of Thin Film Encapsulation (TFE) Material.....	10
1.5 Methods of Water Vapor Transmission Rate (WVTR) Measurement.....	14
1.5.1 MOCON Measurement.....	14
1.5.2 Calcium (Ca) Test.....	15
1.5.3 Tritiated Water (HTO) Test.....	16
1.6 Plasma.....	18
1.6.1 Direct Current (DC) Plasma	19
1.6.2 Radio Frequency (RF) Plasma	19
1.7 Plasma-Enhanced Chemical Vapor Deposition (PE-CVD).....	21
1.7.1 Classical Approach of PE-CVD.....	21

1.7.2 Non-Classical Approach of PE-CVD.....	24
1.8 Magnetron Sputtering.....	30

Chapter2. Effects of RF power and gas ratio on barrier properties of SiO_xN_y films deposited by inductively coupled plasma chemical vapor deposition.....

2.1 Introduction.....	34
2.2 Experimental.....	36
2.3 Results and Discussion.....	37
2.4 Conclusion.....	49

Chapter3. Permeation barrier properties of silicon oxide films deposited on polyethyleneterephthalate (PET) substrate using roll-to-roll reactive Magnetron sputtering system.....

3.1 Introduction.....	50
3.2 Experimental.....	52
3.3 Results and Discussion.....	54
3.4 Conclusion.....	64

Chapter4. Improvement of NiMoNb to polyimide adhesion by inductively coupled nitrogen plasma treatments (Independent Topic)...	67
4.1. Introduction.....	67
4.2 Experimental.....	69
4.3 Results and Discussion.....	70
4.4 Conclusion.....	80
Reference.....	82
국문초록.....	90

List of Figures

Figure 1 Structure of OLED device.

Figure 2 Trend of flexible OLED mobile display.

Figure 3 Type of (a) glass (metal) and (b) thin film encapsulation.

Figure 4 Penetration paths of water and oxygen through passivation membrane.

Figure 5 Equation showing the factors affecting the diffusion and the process of penetration of moisture into the barrier surface.

Figure 6 Change of characteristics over time of OLED devices with poor sealing.

Figure 7 Organic/inorganic hybrid encapsulation film.

Figure 8 WVTR measurements of (a) MOCON, (b) Ca test, and (c) tritiated water test.

Figure 9 Classical approach of PE-CVD.

Figure 10 Non-classical approach of PE-CVD based on the theory of charged nanoparticle.

Figure 11 Differences in deposition behavior by substrate type (a) diamonds deposited on Si substrates (b) carbon soot stacked on Fe substrates.

Figure 12 Mass distributions of negatively charged nanoparticles according to the change of methane concentration in low pressure diamond deposition process using HW-CVD.

Figure 13 Silicon nanoparticles captured in the vapor phase during silicon deposition.

Figure 14 Schematic diagram of DC magnetron sputtering system.

Figure 15 Schematic of the ICP-CVD system.

Figure 16 FE-SEM cross-section images of SiO_xN_y films deposited at Ar/SiH₄, O₂/(O₂+N₂) of 4.5 and 0.1, respectively with RF power of (a) 0.5 kW, (b) 0.7 kW (c) 0.9 kW and (d) at Ar/SiH₄, O₂/(O₂+N₂) of 41 and 0.1, respectively with RF power of 0.9 kW.

Figure 17 Effect of Ar/SiH₄ ratio and RF power variation on the density and WVTR of 100 nm-thick SiO_xN_y films deposited using O₂/(O₂+N₂) ratio of 0.1.

Figure 18 Si 2p core-level XPS spectra of 100 nm-thick SiO_xN_y thin film deposited at Ar/SiH₄ and O₂/(O₂+N₂) of 4.5 and 0.1, respectively, with RF power of 0.9 kW.

Figure 19 Ca test results of 100 nm-thick SiO_xN_y films deposited at Ar/SiH₄, O₂/(O₂+N₂) of 4.5 and 0.1, respectively with RF power of (a) 0.5 kW, (b) 0.7 kW (c) 0.9 kW and (d) at Ar/SiH₄, O₂/(O₂+N₂) of 41 and 0.1, respectively, with RF power of 0.9 kW.

Figure 20 STEM images of primary nanoparticles captured at Ar/SiH₄ and O₂/(O₂+N₂) of 4.5 and 0.1, respectively, with RF power of (a, e) 0.5 kW, (b, f) 0.7 kW (c, g) 0.9 kW and (d, h) at Ar/SiH₄ and O₂/(O₂+N₂) of 41 and 0.1 with RF power 0.9 kW. (e), (f), (g) and (h) are magnified images respectively of the boxes in (a), (b), (c) and (d).

Figure 21 STEM Image and size distribution of primary nanoparticles captured at 0.9 kW with Ar/SiH₄ and O₂/(O₂+N₂) of 41 and 0.1, respectively.

Figure 22 STEM images of primary nanoparticles captured at Ar/SiH₄ and O₂/(O₂+N₂) of 41 and 0.1, respectively, with RF power of (a, e) 0.3 kW, (b, f) 0.5 kW (c, g) 0.7 kW and (d, h) 0.9 kW. (e), (f), (g) and (h) are magnified images respectively of the boxes in (a), (b), (c) and (d).

Figure 23 Behavior of Growth rate of SiO_xN_y films as a function of RF power at Ar/SiH₄ and O₂/(O₂+N₂) of 4.5 and 0.1, respectively.

Figure 24 WVTR and residual stress of SiO_xN_y films deposited at Ar/SiH₄ and O₂/(O₂+N₂) of 41 and 0.1, respectively, with RF power of 0.9 kW as a function of film thickness.

Figure 25 OM images of (a) 300 nm-thick SiO_xN_y film, (b) 400 nm-thick SiO_xN_y film deposited at Ar/SiH₄ and O₂/(O₂+N₂) of 41 and 0.1, respectively, with RF power of 0.9Kw.

Figure 26 Schematic diagram of the roll to roll dual magnetron sputtering system to deposit the SiO_x films.

Figure 27 Change in the WVTR and O/Si atomic ratio of the 100 nm-thick SiO_x barrier films deposited on 50 μm-thick PET substrate as a function of O₂ flow ratio.

Figure 28 Optical transmittance of 100 nm-thick SiO_x film prepared by reactive sputtering according to O₂ content.

Figure 29 Change in the WVTR and residual stress of 100 nm-thick SiO_x films deposited on 50 μm-thick PET substrate as a function of sputtering power.

Figure 30 Surface roughness and density of 100 nm-thick SiO_x films fabricated using various sputtering power.

Figure 31 AFM image showing the surface roughness of 100 nm-thick SiO_x films deposited as a function of sputtering power (a) 3.0 kW, (b) 5.0 kW, (c) 7.0kW

Figure 32 Change in the WVTR and residual stress of the barrier films deposited on 50 μm -thick PET substrate as a function of film thickness.

Figure 33 TEM micrograph of the SiO_x films deposited on PET substrates using (a) 5 % O₂/95 % Ar at the power of 3.0 kW and (b) 15 % O₂/85 % Ar at the power of 5.0 kW

Figure 34 Change in the WVTR and residual stress of the SiO_x barrier film as a function of the number of passes of web at constant total film thickness with 300 nm

Independent Topic

Figure 35 Peel strengths of the FCCLs according to the sputtering power of the NiMoNb adhesion layer.

Figure 36 Density of NiMoNb adhesion films according to the sputtering power.

Figure 37 Peel strength of the FCCLs treated plasma as a function of RF power before NiMoNb deposition.

Figure 38 Relationship between the surface roughness and RF power.

Figure 39 XPS C 1s spectra of the fractured PI surface for two samples: (a) 200 W and (b) 900W.

Figure 40 Cross-sectional HR-TEM image obtained from (a) 200 W plasma-pretreated FCCL samples, (b) 200 W plasma-pretreated FCCL samples subjected to annealing at 150°C for 24 h, (c) 900 W plasma-pretreated FCCL samples, (d) 900 W plasma-pretreated FCCL samples subjected to annealing at 150°C for 24 h.

List of Tables

Table 1 XPS C 1s spectra of the plasma treated two FCCL: (a) 200 W, (b) 900 W.

1.1 Basic Principle and Structure of OLED Device

Since the light-emitting principle of OLED is electroluminescence, it emits a light when electrons and holes meet. Basically, OLEDs emit light in what's called an 'emission material layer' (EML), which is made up of light-emitting materials that react when a current is applied. It has higher luminous intensity than preexisting inorganic light emitting diodes and can emit light efficiently at low voltage. Because of its excellent characteristics and advantages such as high contrast ratio, ultra-fast response time, low power consumption, wide viewing angle, research of OLED, especially flexible OLED has been widely studied by many research groups.

As shown in Fig. 1, the organic EL (electroluminescence) display has an anode, three layers of organic films (hole transporting layer, light emitting layer, electron transporting layer) and cathode are laminated in this order. When an organic molecule receives energy (excitation state), it tries to return to its original state, and the energy received then is emitted as light.

When power is supplied, electrons move and current flows. On the cathode, electrons with the help of the electron transporting layer, they move to the light emitting layer. On the anode, holes moved to the light emitting layer with the help of the hole transporting layer. Electrons and holes encountered in the organic light emitting layer generate high energy excitons, at this time, excitons fall to low energy level and generate light.

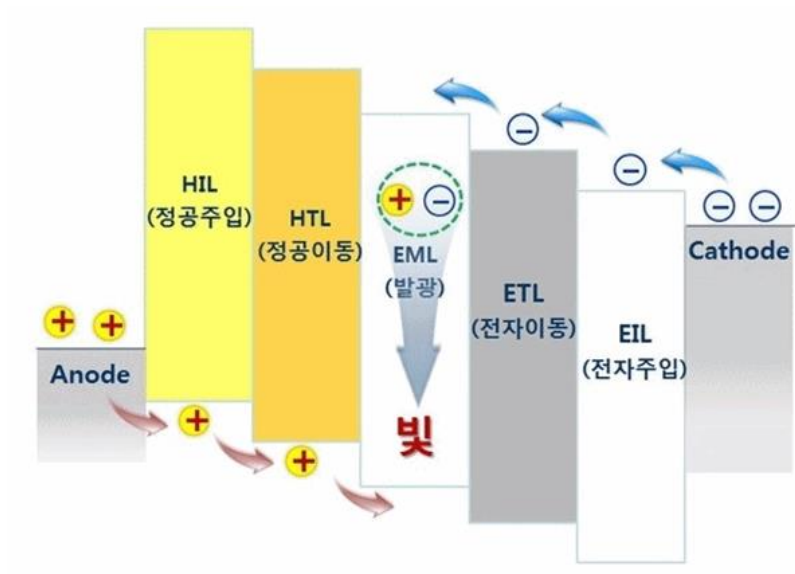


[Figure 1.] Structure of OLED Device.

1.2 Issue of Flexible OLED Display

Recently, organic light emitting diodes (OLEDs) have received a great deal of attention for large area display due to their advantages of fast response time, flexibility, high brightness, and color tenability[1-5]. Especially, OLEDs deposited on plastic substrates such as polyethylene terephthalate (PET), polyethylene naphthalate (PEN), and polycarbonate (PC) have attractive potentials due to robust profile, light-weight, their ability to curve, fold, roll, and design freedom [6-9]. However, the main problem of flexible OLEDs is the reliability and long term stability. Degradation of OLED properties has been attributed to various mechanisms such as electrochemical reactions at the electrode/organic interface [10], cathode oxidation[11, 12], crystallization of the organic solids[13], and migration of ionic species [14]. Among these, the cathode oxidation was shown to be mainly responsible for the growth of dark non-emissive spots [15]. Thus, to fabricate reliable and high performance flexible OLEDs, it is imperative to obtain encapsulation layers resistant to permeation of moisture and oxygen. For this reason, many encapsulation techniques such as sputtering [16-18], chemical vapor deposition (CVD) [19-25], and atomic layer deposition (ALD) [26-29], have been widely studied in terms of the long-term stability of OLEDs. Many research groups have tried to design the proper means of encapsulation. For example, Barix coating which is composed of alternating organic-inorganic multilayers has been reported; however it is difficult to be employed in mass production of OLEDs because of complicate and long-time process [30]. The application of the ALD process is limited because of extremely low deposition rates about $1 - 3 \text{ \AA}/\text{cycle}$ although a barrier film deposited by ALD usually shows a much better water vapor transmission rate (WVTR)

than that of a barrier film deposited by sputtering or CVD processes and ALD has the inherent advantages to deposit very dense films [31].

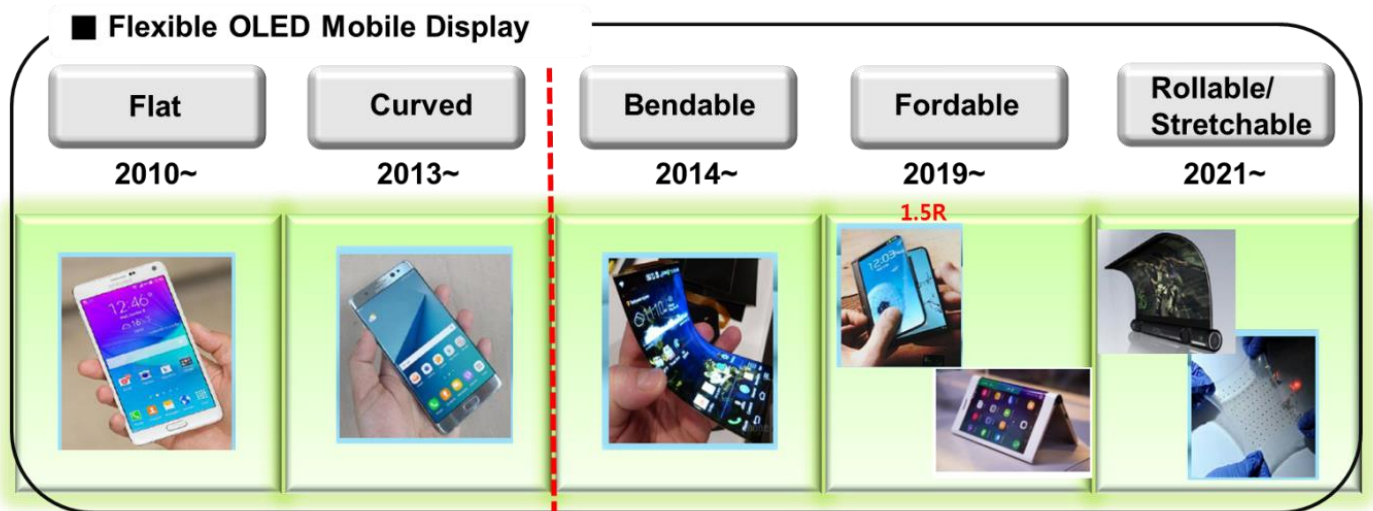


[Figure 2.] Trend of Flexible OLED Mobile Display.

1.3 Encapsulation of OLED Display

In the past, glass lid and metal cap methods have been used for encapsulating OLED displays. This process is a method of applying UV Epoxy resin with low moisture permeability to the edge of the OLED display device and covering the metal or glass can. In addition, getter was put in the space between lid and OLED display device to remove residual moisture to minimize the moisture [32-34]. The method using the double metal can has been used in the early small PM-OLED because it has advantages in terms of manufacturing cost due to its strength and process shortness compared to the glass can.

However, if the quality is not uniform as bending and cutting the stainless steel plate of 200um thickness by the general press working, the sealing property is deteriorated, and there is a problem that it is difficult to apply the panel because it is somewhat separated from the heat deformation characteristics. In addition, due to the opaque characteristics of the metal can itself, there was a disadvantage that the front emission of the display is impossible. In this respect, the use of Glass Lid has the advantage that both front and back light emitting displays are available. However, most of the recently produced Mobile OLED displays are released in the form of thin bezels and high resolution, making it difficult to manufacture modules with a back-emitting OLED structure.

Therefore, in recent years, most small AMOLEDs are manufactured with a top emitting OLED structure, and since light must be extracted upward, it is difficult to apply a metal can, and thus glass is used. However, glass also cannot be applied to flexible displays, so it cannot be used as an encapsulation technology. To solve this problem, the encapsulation technology of the flexible OLED display has developed into a thin film

encapsulation technology. However, unlike metal can and glass, it is very difficult to realize WVTR 1×10^{-6} g / m² day required by OLED display by depositing single layer inorganic thin film. Inorganic thin films grow mostly in columnar structure during thin film growth, and when some pinholes are introduced, this part acts as a defect, and when moisture approaches, it moves easily toward the OLED material through the defect.

For reference, oxygen molecules are usually 4 Å and water molecules are 5 Å in size. The penetration of these molecules is known to be proportional to the solubility at the surface of the gas barrier and the diffusion constant in the film, as shown in the following equation. It is also known that the total flow rate of oxygen or moisture is proportional to the difference in oxygen or moisture concentration at both sides of the barrier film, and depends on the partial pressure difference between the two. That is, if the pin hole is present in the thin film formed by the gas barrier, water and oxygen molecules cannot be prevented from penetrating into the device according to the diffusion law due to the concentration gradient, and when these molecules enter the OLED device, OLED device is degraded. Direct degradation of OLED devices is due to oxidation of the Al electrodes due to oxygen or water molecules, exfoliation, and oxidation and crystallization of organics. This degradation can occur much faster under water vapor.

In order to suppress pinhole generation which causes these problems, it is necessary to establish an optimized thin film process and deposit a high density inorganic thin film. Nevertheless, as mentioned above, it is difficult to secure WVTR 10^{-6} g / m² day with a single thin film, and an inorganic / organic / inorganic multilayer thin film structure is applied to the flexible OLED display that is currently commercialized. . This structure

does not completely block moisture or oxygen molecules, but may delay the time that the moisture or oxygen molecules are absorbed on the surface of the encapsulation material and diffuse to the device as much as possible.

In the case of inorganic film deposition, researches using CVD and ALD technologies are actively conducted, and in the case of organic film deposition, researches on thermal evaporator or inkjet printing technology are being actively conducted.

In terms of mass production, the rapid development of technology and the development of technology capable of depositing high density thin films with low defects at a thin thickness are emerging as a key issuer.

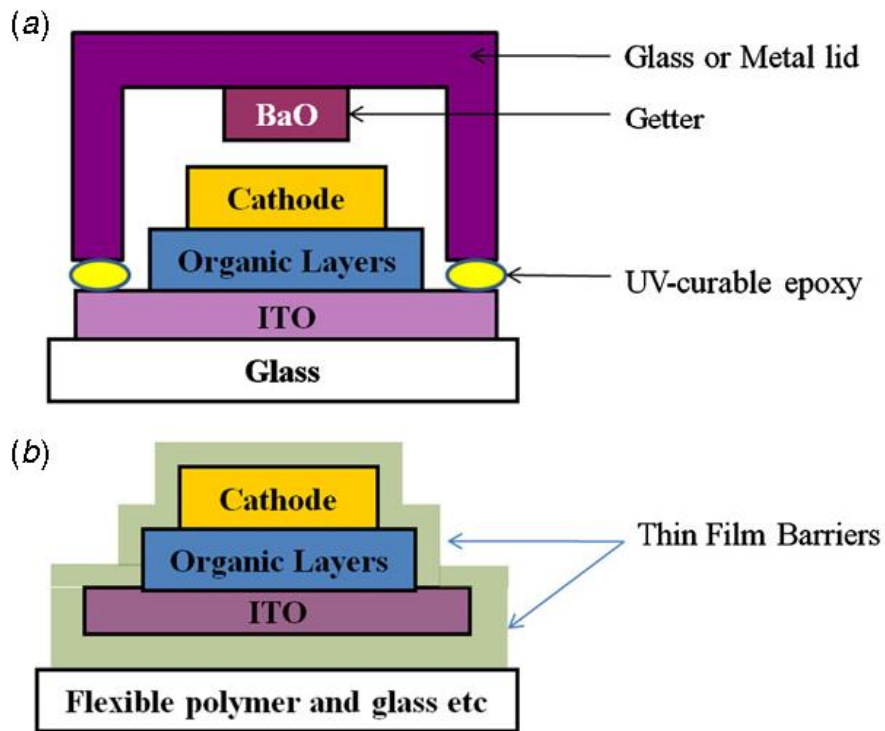


[Figure 3.] Type of (a) Glass (Metal) and (b) Thin Film Encapsulation.

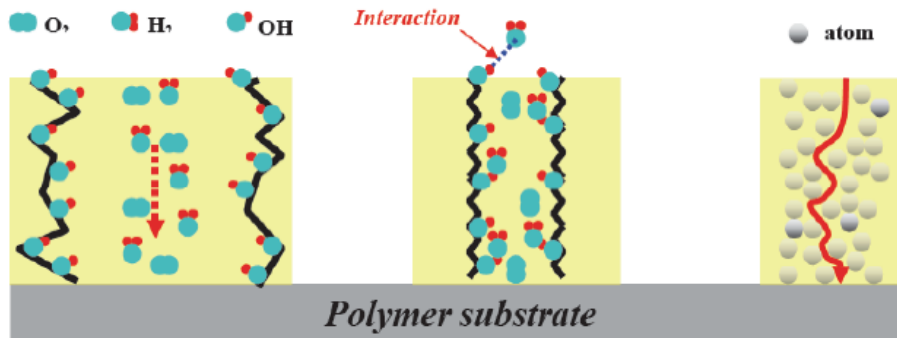


[Figure 4.] Penetration Path of Water and Oxygen Through Passivation Membrane.

$$P = S \times D$$

P : Permeation coefficient (permeability)

S : Solubility coefficient, determine how much of the permeant can be dissolved in the film

D : Diffusion coefficient, determines how fast the permeant can move in the media

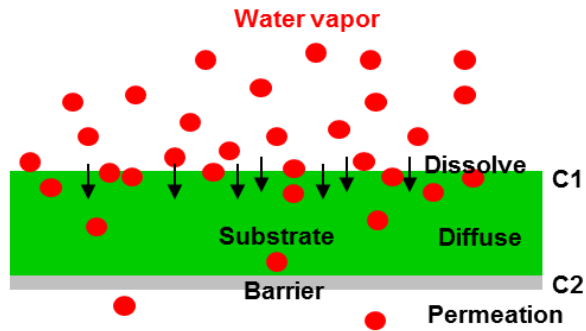


[Figure 5.] Equation Showing the Factors Affecting the Diffusion and the Process of Penetration of Moisture into the Barrier Surface.

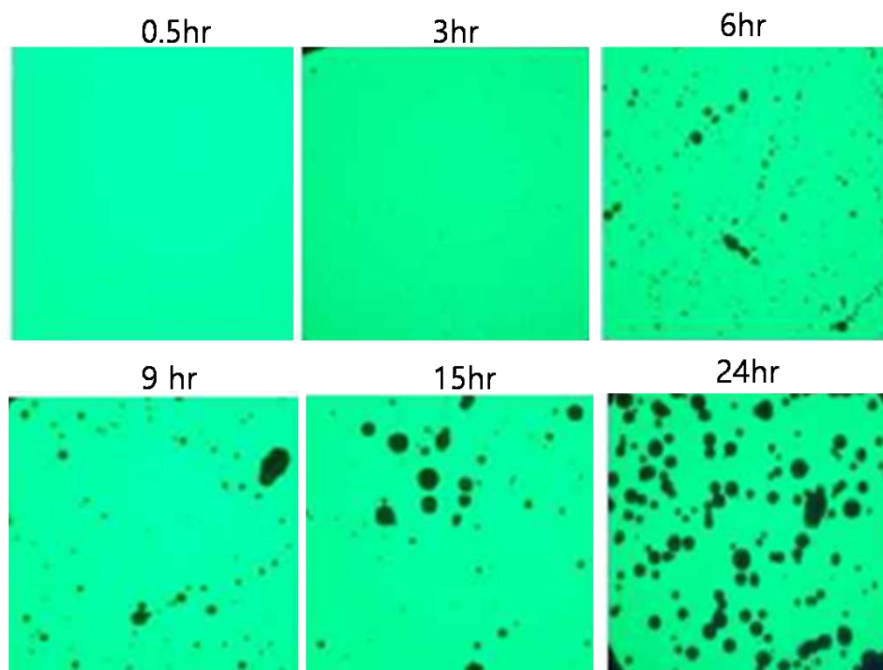


[Figure 6.] Change of Characteristics over time of OLED Devices with Poor Sealing.

1.4 Consideration of Formation of TFE

In order to satisfy the low water vapor transmission rate (WVTR) required for OLEDs, it is necessary to form an encapsulation film in consideration of various characteristics such as deposition equipment for forming an encapsulation film, establishment of optimized process conditions, mass production, encapsulation film structure, and material properties.

First, in order for the encapsulation film developed by R & D to be applied in mass production in the future, the encapsulation film characteristics and deposition rate (productivity) must be considered. No matter how good the encapsulation film characteristics, if the deposition rate is too slow, it will not be practical to use due to the increased cost for mass production facilities. In this aspect, in the case of atomic layer deposition technology (ALD), a material is deposited in an atomic layer to form an encapsulation film having excellent characteristics with a very low defect density [22]. However, the low deposition rate of 0.1-0.2nm / cycle is not currently used in mass production. So far, the encapsulation film characteristics are somewhat inferior, but PECVD equipment with a deposition rate of 100-200nm / min is used in mass production, and it is continuously researching equipment development and process optimization to improve the encapsulation film properties by PECVD [3].

Second, in encapsulation, it is necessary to consider encapsulation material (Al_2O_3 , SiO_x , SiN_x , SiO_xN_y , MgO , ZrO_2 , ZnO) and encapsulation film structure (inorganic, inorganic / organic composite structure) [3, 22, 35]. As mentioned above, it may be best to use an inorganic film made of a high density material. However, it is difficult to use only an inorganic film that lacks flexibility to apply a flexible OLED display. The

method devised to solve this problem is the organic / inorganic hybrid structure presented by Vitex. In this structure, a high density inorganic film that prevents water permeation and an organic film are laminated several times in order to ensure flexibility. This is a structure that can compensate for defects in the inorganic layer formed by impurities during the process with a multilayer film structure and also secure the flexibility of the encapsulation film. In the organic / inorganic multilayer structure as shown in Fig. 1.8, the water permeation path occurs in the inorganic layer defect. If the number of defects per layer is small enough, the path of moisture transmission can be expressed as the product of the distance between each defect and the number of layers. In addition, since the effective thickness can be made as long as possible by lengthening the path of permeated water, the organic / inorganic multilayer structure is currently used in most production processes.

Third, the encapsulation film must have a large polarity to effectively block water permeation, because water with a large dipole moment interferes with the continuous permeation of water while forming OH groups on the surface of the oxide film and the pores with high polarity. Since the polarity can be estimated as the refractive index, consideration of an encapsulation film having a large refractive index is required.

Fourth, most of small and medium sized displays have a top light emitting structure, so the encapsulation film should have excellent optical transmittance in order to be applied to flexible displays using top-emission OLEDs and polymer substrates. Unlike bottom-emission structured OLEDs of large displays emitting light through transparent glass substrates, top-emission OLEDs are very important for the integration of OLEDs with electronic devices. Top emission is desirable for active-matrix OLEDs because all circuits can be placed on the bottom without any interference from components such as

transistors or wires. It is possible to modulate the optical properties of emitted light by using a micro-cavity structure that requires a transparent thin film having a high refractive index. Therefore, a transparent encapsulation film having a high refractive index is advantageous.

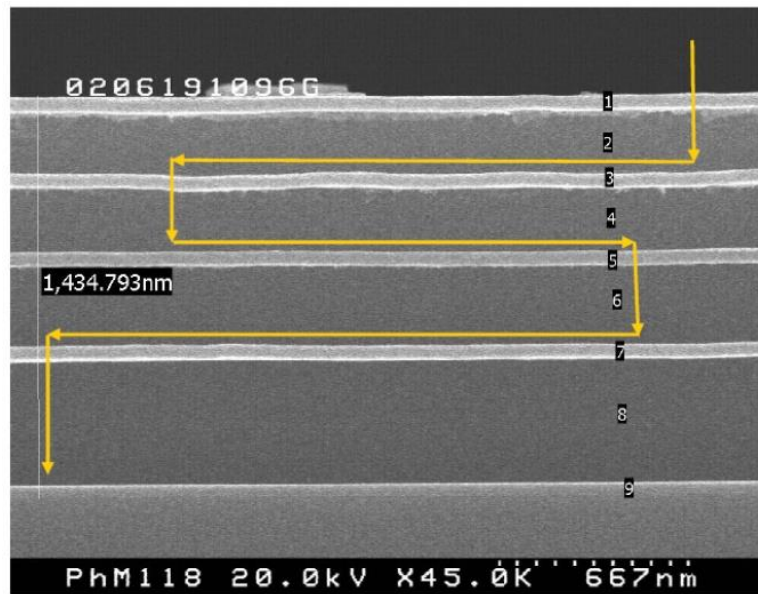
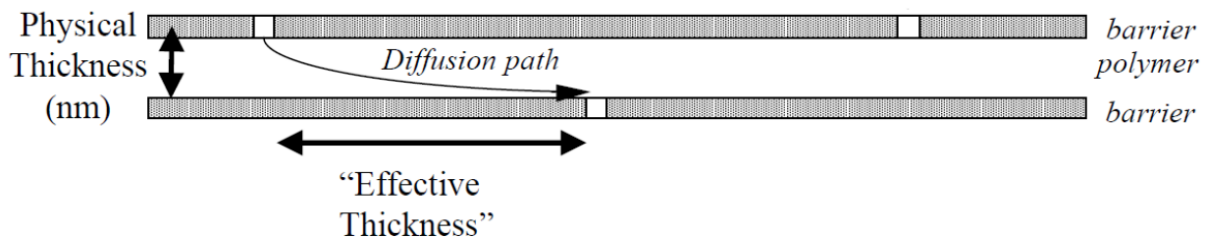


[Figure 7.] WVTR Organic/Inorganic Hybrid Encapsulation Film.

1.5 Methods of Water Vapor Transmission Rate (WVTR) Measurement

1.5.1 MOCON Measurement

The most common way to measure the water vapor transmission rate (WVTR) is to use commercially available equipment from MOCON [36]. In the early days, MOCON, which was manufacturing equipment to measure the moisture permeability of food packaging films, has gradually expanded its business to equipment for measuring the moisture permeability of encapsulation films for flexible OLED displays. Initial moisture permeability measurement equipment was developed for food packaging film, so the moisture permeability below $10^{-2} \text{ g} / \text{ m}^2 \cdot \text{ day}$ could not be measured, but many developments have been completed. Moisture permeability can be measured until $10^{-5} \text{ g} / \text{ m}^2 \cdot \text{ day}$. The principle of measurement is to fix the film to be analyzed in the holder and to continuously spray the fixed quantity of water to one side, and then the sensor captures the amount of moisture penetrated through the film and quantifies it. As it is a commercialized equipment, it has been evaluated as the most reliable method to measure moisture permeability until now, but the disadvantage is that equipment capable of measuring moisture permeability up to $10^{-5} \text{ g} / \text{ m}^2 \cdot \text{ day}$ range is very expensive and the measurement is impossible for the range below $10^{-5} \text{ g} / \text{ m}^2 \cdot \text{ day}$,

1.5.2 Calcium (Ca) Test

The next method is to measure the water vapor transmission rate using the degree of oxidation of calcium. Calcium is known as a substance that reacts well with moisture, and can be used as a substance to measure the amount of moisture passing through the encapsulation film. The method of measuring moisture permeability using calcium is largely dependent on the degree of oxidation of calcium.

It can be divided into a method using a change in other light transmittance and a method using a change in electrical properties. First, it is a method of detecting the change of light transmittance according to the oxidation degree of calcium. The deposited calcium is silver, but when it reacts with moisture, it is transformed into calcium oxide and becomes transparent. Depending on the amount of moisture entering through the encapsulation film, the rate of calcium transparent can be analyzed with a light transmittance measuring device to quantitatively analyze the amount of water passing through the encapsulation film.

The second method is to use the electrical properties of calcium [37]. Since calcium has a metallic property immediately after deposition, it has conductor properties, but after being transformed into calcium oxide by combining with water, it has properties of inorganic materials and high resistance non-conductors. This method combines the encapsulation film on the previously deposited electrode and calcium, and applies a constant voltage to both electrodes to quantitatively analyze the resistance or current change over time to measure the amount of moisture that has penetrated the encapsulation film.

There are many opinions that it is somewhat less reliable than commercial products of

MOCON, but since it is relatively inexpensive and easy to access, it is preferred by small research groups and universities

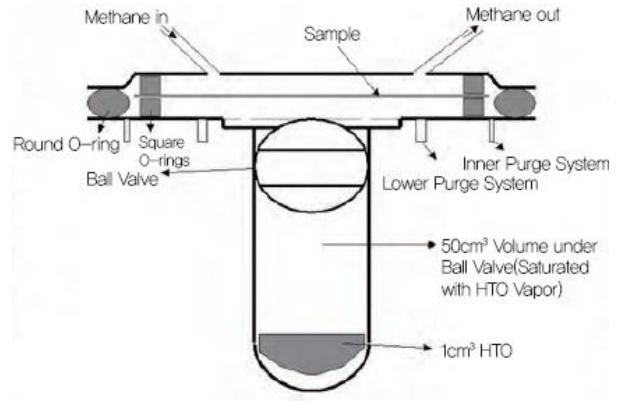
1.5.3 Tritiated Water (HTO) Test

The next method is to measure the moisture permeability using tritium, a radioisotope. In Korea, it is mainly carried out by Korea Research Institute of Standards and Science. This is a method of measuring the moisture permeability of the encapsulation film by incorporating tritium into water molecules and then spraying it on the film, and detecting the amount of water including tritium in the water passing through the film with a radiation detector. It can measure up to $10^{-7} \text{ g} / \text{m}^2 \cdot \text{day}$, so it can measure ultra-small amount of water that has passed through the encapsulation film. However, there are disadvantages that the equipment is expensive and not many institutions use this method to measure moisture [38, 39].

(a)



(b)



(c)

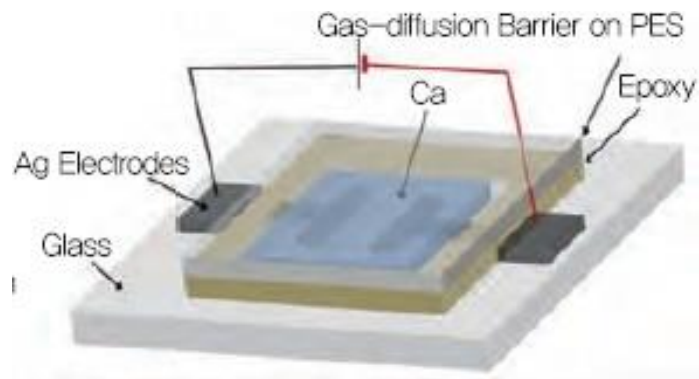


[Figure 8.] WVTR Measurement of (a) MOCON, (b) Ca Test, and (c) Tritiated

Water Test.

1.6 Plasma

Plasma refers to an electrically neutral, partially ionized gas. Of course, this gas contains neutral elements, electrons, ions, excited neutral elements, and photons, and in the case of molecular gas, there is a radical that is a gas from which molecular gas is decomposed. The ionization rate of the neutral element in the plasma is about 10^{-7} - 10^{-3} , and the ionization rate is very small. In the plasma, the electron density and the ion density are almost the same. Therefore, plasma is also a conductive gas through which electricity flows due to the presence of neutral or electron ions, and the charges move according to the electric field present inside. The electrons and ions in these plasmas are produced by the ionization process, or recombine with other ions and move to the chamber wall and disappear. Electrons and ions that are adjacent to each other in the plasma are likely to be neutralized by electrostatic interaction, but when one electron is seen, other ions exist in each direction, so there is an electrostatic force due to these ions. Therefore, the electrostatic forces of each other cancel, so that the electrons or ions in the plasma behave like free particles without static electricity from the surroundings, just like neutral elements. In addition, as mentioned above, when electrons in an atom are excited to a high energy level and move back to a low energy level, light is emitted [40].

1.6.1 DC Plasma

A few ways to transfer energy to electrons are as follows: First, a DC voltage between electrodes is applied to create an electric field in the space to give energy to the electrons. This is called DC plasma or DC glow discharge plasma. In this case, free electrons and secondary electrons from the electrode, sometimes hot electrons generated by increasing the temperature of the electrode, help the free electron alone to act as a factor to form high-density plasma. From this point of view, it can be said that the type of electrode also greatly affects plasma generation and maintenance.

Here, in the plasma, the electric field is very small and the actual electric field is very near the negative electrode, so most of the electrons are accelerated in the negative electrode sheath region.

1.6.2 RF Plasma

There is a method of accelerating electrons from an electric field that changes with time by applying RF to both electrodes. The electrons are accelerated from the electric field formed in the space, and when plasma is formed, the electrons are accelerated in the sheath region near the electrode as above, and since the sheath oscillates with time, electrons entering the sheath bounce back as the sheath changes. Electrons are more effectively energized by the effect of gaining energy, i.e. by hitting flying balls. These play a big role in the ionization reaction. The resulting plasma can form higher density plasma than the DC plasma. The plasma equipment that produces this is called capacitively coupled plasma (CCP).

A more efficient way of energizing electrons is by using induction electric fields [41]. In the above methods, the electric field starts from the electrode and ends with the electrode, so the path of the electric field is limited. However, an inductive field results in the termination of electric fields in the space. The induced electric field is formed by the alternating current flowing in the antenna in time, and the magnetic field is changed in time (Amp Ampere), and the induced electric field is formed around the magnetic field (Faraday Law). It can be accelerated independently of the electrode. This plasma is called inductively coupled plasma, ICP [42]. The structure is designed to isolate the reactor and antenna from the dielectric and to introduce electromagnetic fields from the antenna into the reaction. Not only does high current flow through the antenna, it also takes a high antenna potential. Considering that the power applied to the antenna is the product of the current and the voltage, the role of power will make the above inductive electric field by the current, and the antenna potential will make the electric field perpendicular to the dielectric plane. The latter is similar to the CCP plasma as described earlier. Therefore, in ICP plasma, the inductive electric field effect (H-mode) and the capacitive electric field plasma is formed from the effect (C-mode). Here, the C-mode mainly plays an important role in the initial ICP discharge, and then high density plasma is formed by H-mode.

1.7 Plasma Enhanced- Chemical Vapor Deposition (PE-CVD)

1.7.1 Classical Approach of PE-CVD

Plasma Enhanced Chemical Vapor Deposition (PECVD) technology is widely used in display devices and solar cells because it can deposit semiconductor and dielectric thin films at low temperature at a relatively low cost in large area. In PECVD system, gas is ionized and activated by electric field. Plasma is the fourth state of a solid, liquid, and gas followed by a gas that is weakly ionized by energy and exhibits completely different physical properties from the gas state. Typically, the degree of ionization in the total gas is less than 1%, so only a small part of the input gas is deposited in the form of a thin film. The sequence of reactions of typical PECVD that has been around for decades is as follows.

The mechanism of thin film formation by PECVD is

1. The reactants are transferred to the substrate region.
2. These are transferred to the substrate surface on which they are adsorbed.
3. After surface adsorption, the reactants move over the surface in an unstable state to reach a ledge or kink site.
4. As the epitaxial layer grows, chemical reactions such as catalysis at the surface occur.
5. The gas product is removed from the main gas stream.
6. The reaction product is removed from the reactor.

Under typical PECVD conditions, the energy of the electrons is small enough that the radical formation rate is faster than the ionization rate. In addition, the radical has a high adsorption coefficient, so it is easily adsorbed on the surface, and then finds and moves to the most stable site to form new bonds.

In general, PECVD process variables are the distance between electrodes, substrate temperature, pressure, power, gas flow rate and gas composition ratio. A typical PECVD apparatus has a planar planar structure and the wafer is placed on the ground electrode to minimize the sputtering effect of ion bombardment. After the PECVD process, the thin film characteristics were analyzed by ellipsometer, XRR, XRD, XPS, FESEM, etc. for analyzing film thickness non-uniformity, density, refractive index, composition ratio, deposition rate, and residual stress.

PECVD is widely used in the industry because it can deposit high quality thin film at low temperature compared with thermal CVD.

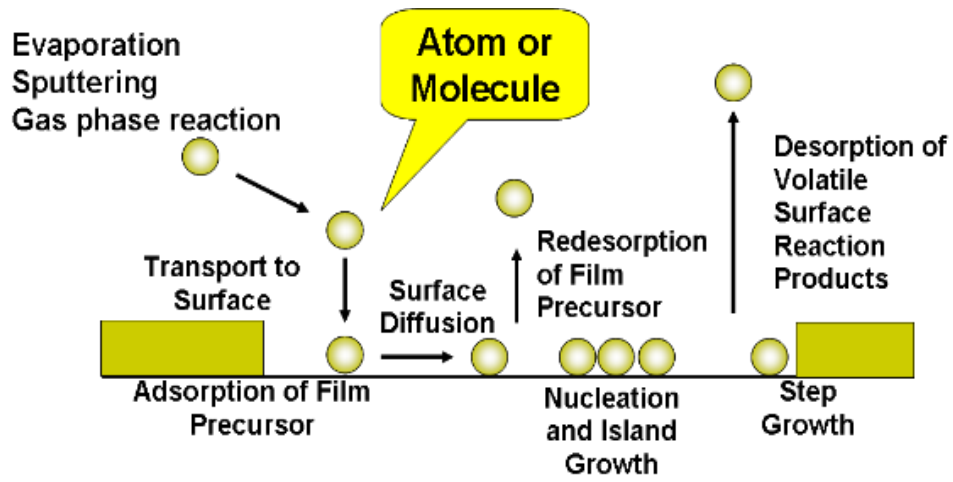


[Figure 9.] Classical Approach of PE-CVD.

1.7.2 Non-Classical Approach of PE-CVD

The conventional CVD thin film growth described above is that after the atoms of gaseous phase are adsorbed onto the substrate, they move around the surface in an unstable state, reach the ledge or kink site, and then form the thin film through nucleation formation, island growth, coalescence, etc. In actual thin film processes, however, there are many phenomena that cannot be explained by the theory of crystal growth by atoms. A representative example is that of diamond growth, as shown in Fig. 11. When the general diamond deposition conditions were applied to two kinds of Si and Fe substrates, diamond was well deposited on the Si substrate, but porous soot was formed on the Fe substrate instead of diamond [43]. In the case of deposition by atoms, because it forms atomic bonds, a weak bonding material such as soot cannot be deposited. Thus, the formation of soot on Fe substrates in low-pressure diamond CVD processes cannot be explained by the TLK (Terrace-Ledge-Kink) model, which is a traditional CVD growth deposited by atoms or molecules. In order to understand these phenomena, Hwang Nong-Moon's group has been conducting detailed analysis for a long time to produce various kinds of thin films including diamond thin films produced in chemical vapor deposition process and the main source of deposition of various nanostructures such as nanowires and nanotubes in the gas phase. "Charged nanoparticle theory" is presented [44, 45]. In order to understand these phenomena, Hwang Nong-moon's group conducted a detailed analysis for a long time, and found out that the main source of deposition for various nanostructures such as thin films, nanowires, and nanotubes produced in chemical vapor deposition is because of the charged nanoparticles produced in the gas phase.

From this result, a theory of new CVD thin film growth called, charged nanoparticle theory is presented by Professor Hwang Nong-moon. According to the charged nanoparticle theory, electrically charged nanoparticles are produced first in the gas phase, and these nanoparticles are deposited to grow a thin film. The theory states that when charges are easily dissipated by the substrate when the charged nanoparticles are deposited, van der Waals attractive forces prevail between the particles, causing random Brownian motions, such as flocculation of colloids and then make weak bonds such as soot. On the other hand, if the charge of the particles is maintained on the substrate, electrostatic forces between the particles and the particles or the growth surface are applied, which prevents the particles from randomly dropping and then regular self-assembly may occur, such as colloidal deflocculation. It is said to be able to grow perfect thin films like diamond. On the other hand, if the charge of the particles is maintained on the substrate, electrostatic forces between the particles and the particles or the growth surfaces are applied, which prevents the particles from randomly dropping and regular self-assembly may occur, such as colloidal deflocculation. This leads to grow perfect thin films like diamonds. Sunagawa, Samotoin, and Takamura also reported that thin film deposition units are nanoparticles, not atoms or molecules, but the new paradigm for thin film growth is not easily compatible with previous conventional concepts [46, 47]. Due to these difficulties it received little attention in the field of thin film or the crystal growth. However, since researches on the thin film deposition based on the charged nanoparticle theory have been actively conducted, and various research results have been published, recently it has been greatly recognized.

Observation of charged nanoparticles can be approached in two ways. The first

method is to check the deposition behavior by applying + or – Bias to the substrate by using the fact that the nanoparticles formed in the gas phase are charged. This method is an indirect analysis of the presence of charged nanoparticles, but energy analysis can be used to calculate the number and size of charged nanoparticles present in the gas phase. Second, TEM analysis is performed by capturing nanoparticles in the gas phase. This method can directly identify the nanoparticles present in the gas phase, but the size and number distribution of the particles are not known exactly. Of course, a larger analysis can be used to quantify particle size and number, but it is costly and time consuming. Therefore, in the case of TEM analysis, it is useful to precisely analyze the actual particle shape and crystallinity of charged nanoparticles.

Fig. 12 shows the mass distribution of charged carbon nanoparticles measured in a Hot-Wire CVD (HW-CVD) low pressure diamond process using this energy analyzer. The results show that the diamond process is mostly negative in the gas phase. It can be seen that charged nanoparticles are present. In addition, when the concentration of methane is 1% and 1.5%, the charged nanoparticles are composed of hundreds of carbon atoms, whereas when the concentration of methane is 3% and 5%, the particles having more than 1000 carbon atoms are also present. The higher the concentration of methane, the larger the amount of carbon precipitated in the gas phase, resulting in larger nanoparticles. The size of nanoparticles changes with gas concentration, which is an important factor in determining whether the thin film grows epitaxially or forms grain boundaries. In order to directly identify the charged nanoparticles in the gas phase, the nanoparticles must be captured by the TEM grid. Fig. 13 is a TEM image of Si nanoparticles captured in HW-CVD silicon deposition process. It can be seen that silicon nanoparticles having a size of about 2 to 3 nm exist in the gaseous phase and

other nanoparticles such as ZnO, diamond also has been confirmed a lot [48, 49]. Looking at the cause of the production of these nanoparticles, supersaturation should occur in the gas phase. Supersaturation refers to a condition in which a substance is excessively contained beyond the limit (saturated state) that can be accommodated in the gas phase. Thus, if the substance is in the supersaturated state in the gas phase, it will try to condense into a solid or liquid. The greater the degree of supersaturation, the stronger the degree of condensation. If the degree of supersaturation increases above a certain limit, condensation may occur in the gas phase, leading to the production of nanoparticles. According to Adachi's research, thin films are hardly deposited under conditions in which the supersaturation is weak in the gas phase and nanoparticles cannot be produced [50, 51]. When the nanoparticles are formed due to sufficient supersaturation, deposition occurs. It can be seen that thin film deposition occurs only when nanoparticles are generated. Eventually, the deposition of thin films suggests that the supersaturation is sufficient to produce nanoparticles in the gas phase. This is why nanoparticles are produced in the gas phase in the thin film process.

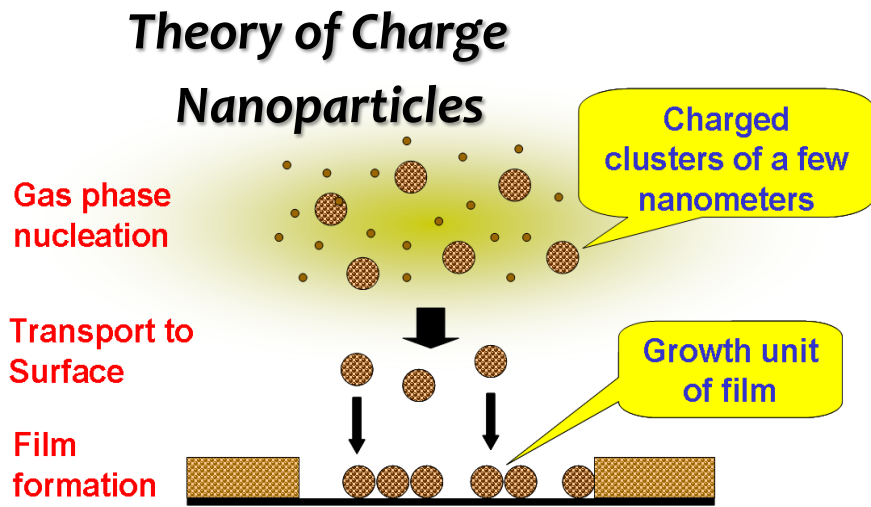


[Figure 10.] Non-Classical Approach of PECVD based on the theory of charged

nanoparticles.

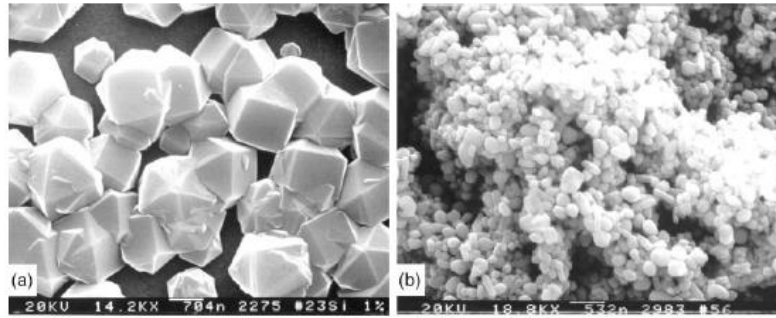


[Figure 11.] Differences in Deposition Behavior by Substrate Type (a) Diamonds Deposited on Si Substrates (b) Carbon Soot Stacked on Fe Substrates.

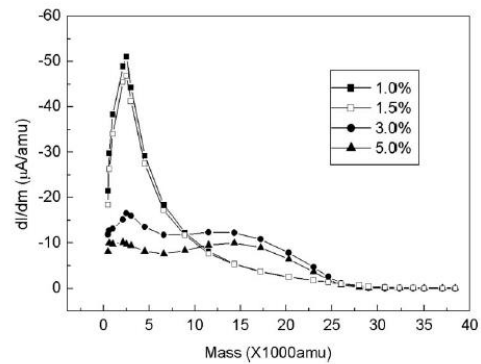


[Figure 12.] Mass Distribution of Negatively Charged Nanoparticles according to the Change of Methane Concentration in Low Pressure Diamond Deposition Process Using HW-CVD.

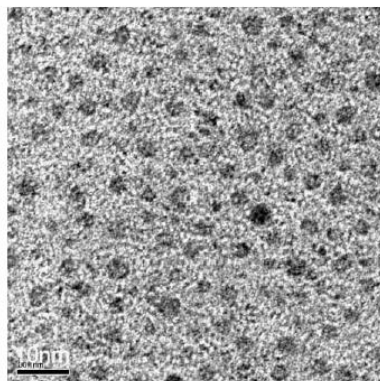


[Figure 13.] Silicon Nanoparticles Captured in The Vapor Phase During Silicon Deposition.

1.8. Magnetron Sputtering

Sputtering begins with the collision between the electrons and the gas supplied into the chamber. In the process, an inert gas such as argon gas is placed in the vacuum chamber (about 1 to 5 mTorr), and when a voltage is applied to the cathode, electrons emitted from the cathode collide with argon gas atoms to ionize argon. Argon + ions in the plasma are accelerated toward the target, which is the cathode by a large potential difference, and collide with the surface of the target to cause neutral target atoms or molecules to stick out to form a thin film on the substrate. When argon ions hit the target material, most of them come out in atomic form (more than about 80% -90%) and the other 10-20% comes out in molecular or cluster form. One of the most important factors in the sputtering process is the sputter rate. The sputter rate is usually proportional to the voltage, i.e., the larger the energy of the Ar cation that strikes the target, the higher the sputter rate. And when this energy is high, the sputtered particles are more likely to have an increased fraction of clusters or molecules than atoms. When the collision energy is low, the target atoms are separated one by one, but as the energy increases, the target is separated into molecules or clusters. This difference is very important because increasing the sputter power can cause large clusters to fall off, which increases the deposition rate and can be productive in terms of productivity, but it can be difficult to control the surface of thin film. When depositing a semiconductor thin film that is sensitive to electrical and optical characteristics, the surface condition can be very different depending on the deposition power. When depositing a semiconductor thin film that is sensitive to electrical and optical characteristics, the surface state of the thin film can vary greatly depending on the deposition power.

Therefore, the process must be performed at an appropriate power without surface damage. If the process is performed at high power considering only productivity in thin film deposition, it is difficult to obtain desired thin film characteristics, especially when depositing a semiconductor thin film. And, control of power is also important when the target is an alloy, compound or ceramic rather than a single material. If the energy of the incident cations is low, the sputtering tends to be sputtered separately into atoms, rather than sputtering into a compound state. At some level of energy, the compound is sputtered into the molecular state. Therefore, if the composition of the thin film formed when using an alloy or compound target differs from the target, it is necessary to consider whether the power is adequate [52]. Such sputtered particles can be detected by using a mass spectrometer near the substrate. When mass spectrometry is used, ions of target substances are detected in the vicinity of the substrate, not neutral atoms, clusters, or molecules. This phenomenon is because sputtered atoms are ionized in the middle or ions have been sputtered from the target. The first sputtered atom is ionized in the middle, which is similar to ion plating. In the case of ion plating, the evaporation material is passed through the plasma to intentionally ionize, and a-bias is applied to the substrate to accelerate the ions to the substrate to increase the adhesion between the thin film and the substrate or the density of the thin film. That is, as the evaporated neutral particles pass through the plasma, ionization occurs due to collision with Ar atoms, Ar cations, or electrons. In the ion plating, the ionization of the neutral atoms passing through the plasma is about 5% or less. Sputtering, like ion plating, causes sputtered particles to reach the substrate as they pass through the plasma, resulting in ionized particles and being able to reach the substrate. Depending on the type and energy size of sputtered particles (atoms, ions, clusters, etc.), the density and surface roughness

characteristics of the deposited thin film are greatly changed, and the electrical and optical properties of the thin film are greatly changed, so it is necessary to adjust the sputter deposition conditions well.

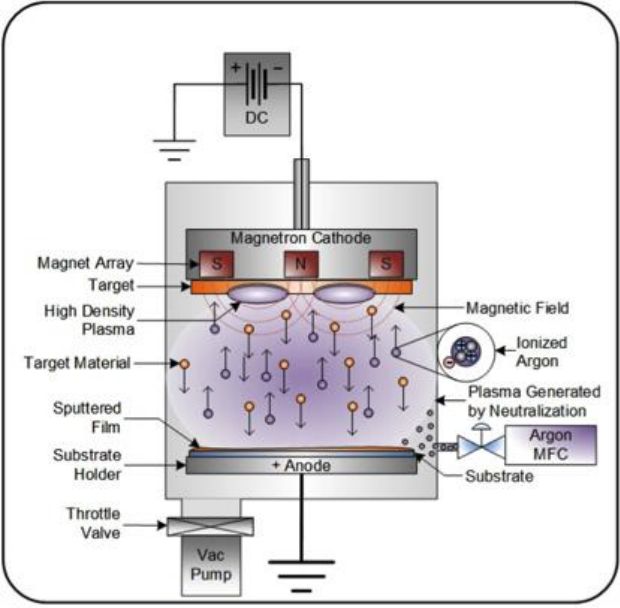


[Figure 14.] Schematic Diagram of DC Magnetron Sputtering System.

Ch. 2 Effects of RF power and gas ratio on barrier properties of SiO_xN_y films deposited by inductively coupled plasma chemical vapor deposition

Introduction

Recently, organic light emitting diodes (OLEDs) have received a great deal of attention for large area display due to their advantages of fast response time, flexibility, high brightness, and color tenability [1-5]. Especially, OLEDs deposited on plastic substrates such as polyethylene terephthalate (PET), polyethylenenaphthalate, and polycarbonate have attractive potentials due to robust profile, light-weight, their ability to curve, fold, roll, and design freedom [6-9]. However, the main problem of flexible OLEDs is the reliability and long term stability. Degradation of OLED properties has been attributed to various mechanisms such as electrochemical reactions at the electrode/organic interface [10], cathode oxidation [11, 12], crystallization of the organic solids [13], and migration of ionic species [14]. Among these, the cathode oxidation was shown to be mainly responsible for the growth of dark non-emissive spots [15]. Thus, to fabricate reliable and high performance flexible OLEDs, it is imperative to obtain encapsulation layers resistant to permeation of moisture and oxygen. For this reason, many encapsulation techniques such as sputtering [16-18], chemical vapor deposition (CVD) [19-21, 23-25, 53], and atomic layer deposition (ALD) [26-29] have been widely studied in terms of the long-term stability of OLEDs. Many research groups have tried to design the proper means of encapsulation. For example, Barix coating which is composed of alternating organic-inorganic multilayers has been

reported; however it is difficult to be employed in mass production of OLEDs because of complicate and long-time process [30]. The application of the ALD process is limited because of extremely low deposition rates about 1 – 3 Å/cycle although a barrier film deposited by ALD usually shows a much better water vapor transmission rate (WVTR) than that of a barrier film deposited by sputtering or CVD processes and ALD has the inherent advantages to deposit very dense films [31]. Since the permeation rate for gasses such as moisture and oxygen depends on the porosity of materials, the deposition of dense encapsulation layers is recognized as a crucial factor for reliable flexible OLEDs. However, there has been little research on the formation mechanism of dense encapsulation films at temperature below 150 °C in CVD systems including an inductively coupled plasma (ICP) CVD system.

In this study, morphology, density and residual stress of films deposited by an internal type ICP-CVD process were analyzed by field emission scanning electron microscopy (FESEM), Rutherford backscattering spectrometry (RBS), laser profile meter. And to investigate the transmitted region of films, calcium (Ca) test was carried out by thermally evaporating Ca on 2x2 in² glass sealed with barrier films and observed by optical microscope (OM).

Besides, we investigated the influence of radio frequency (RF) power and Ar/SiH₄ gas ratio on the behavior of nanoparticles generated in the gas phase and barrier properties. For this, nanoparticles in the gas phase were captured on a membrane of the transmission electron microscopy (TEM) grid and observed by scanning transmission electron microscopy (STEM).

2. Experimental procedure

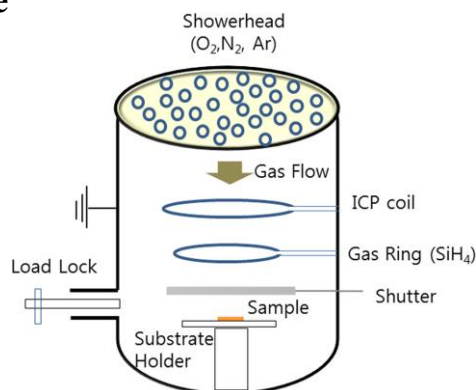


Figure 15 Schematic of the ICP-CVD system.

The schematic of the ICP-CVD reactor is shown in Fig. 1. ICP was produced between the showerhead-type inlet and the substrate by applying RF power through a tuning network to a one-turn coiled copper tube. The coil with a diameter of ~ 100 mm was placed inside the vacuum chamber. Base and working pressures were 1.16×10^{-10} Mpa and 7.90×10^{-7} MPa, respectively. The flow rates of SiH_4 and Ar were varied from 0.8 to 4 standard cubic centimeters per minute (sccm) and from 18 to 33 sccm, respectively, using a mass flow controller (MFC) at a gas ratio of O_2/N_2 of 1:9. The ICP power was varied from 0.3 kW to 0.9 kW and the substrate temperature was maintained at 23°C . The growth rate of SiO_xN_y films was determined by Alpha-Step[®] (ASIQ3) system after averaging at least three measurement data. The cross-section of the SiO_xN_y films was observed by FESEM using a JEOL JSM- 6330F instrument operated at 2.0 kV. The film density was measured by RBS with a beam of He^{+2} particles with average energy of 2.0 MeV. The residual film stress was determined by the beam bending method using a thin film stress measurement instrument (FLX-2320, Tencor), and

derived from the stoney formula. The measurement of WVTR was carried out on a $10 \times 10 \text{ cm}^2$ sample area at $35 \text{ }^\circ\text{C}$ and 90% relative humidity using a WVTR measurement instrument (Deltaperm, Technolox). In order to measure the open pores, which represent a water transmitted region, the calcium (Ca) test was used. In order to check the possibility that nanoparticles should be formed in the gas phase, contribute to film deposition and affect the film morphology as suggested by the non-classical crystallization mechanism of CVD films[54], a TEM grid membrane (C film, 300 mesh copper grid, TED PELLA, INC.) was used to capture nanoparticles under the same condition of film deposition and they are analyzed by TEM using a JEOL 3010F operated at 300 kV. A square stainless-steel shutter was installed 5 mm away from the TEM grid to control the capture time of gas phase nuclei as shown in Fig. 1. In this experiment, the capture time was 5 s.

3. Results and Discussion

Figure 16 shows the FE-SEM image of the cross-section of SiO_xN_y barrier films deposited at powers of (a) 0.5 kW, (b) 0.7 kW and (c) 0.9 kW with Ar/SiH_4 and $\text{O}_2/(\text{O}_2+\text{N}_2)$ gas ratios of 4.5 and 0.1, respectively, and (d) 0.9 kW with Ar/SiH_4 and $\text{O}_2/(\text{O}_2+\text{N}_2)$ gas ratios of 41 and 0.1, respectively. The average film thickness was approximately 100 nm. The porosity of SiO_xN_y films tended to decrease with increasing RF power at Ar/SiH_4 and $\text{O}_2/(\text{O}_2+\text{N}_2)$ of 4.5 and 0.1, respectively. However, the effect on the porosity decrease was only slight with SiO_xN_y films being still porous. A very pronounced effect on the porosity decrease was observed by changing Ar/SiH_4 from 4.5

to 41 as shown in Fig. 16(d), which shows a very dense SiO_xN_y film in contrast with those of Fig. 16(a)-(c).

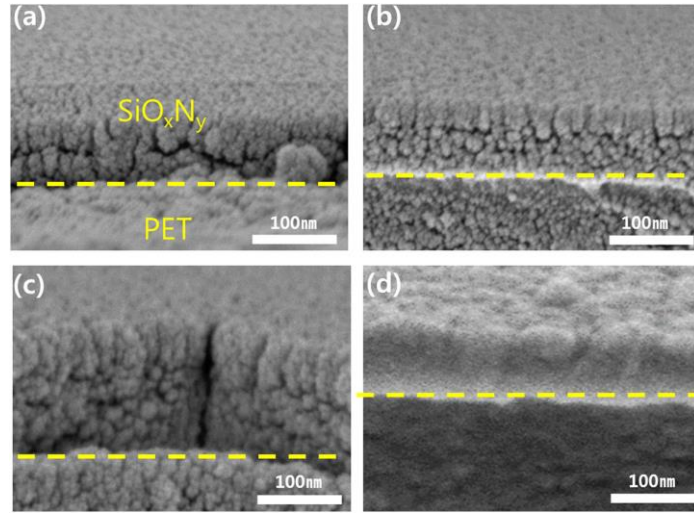


Figure 16 FE-SEM cross-section images of SiO_xN_y films deposited at Ar/SiH_4 , $\text{O}_2/(\text{O}_2+\text{N}_2)$ of 4.5 and 0.1, respectively with RF power of (a) 0.5 kW, (b) 0.7 kW (c) 0.9 kW and (d) at Ar/SiH_4 , $\text{O}_2/(\text{O}_2+\text{N}_2)$ of 41 and 0.1, respectively with RF power of 0.9 kW.

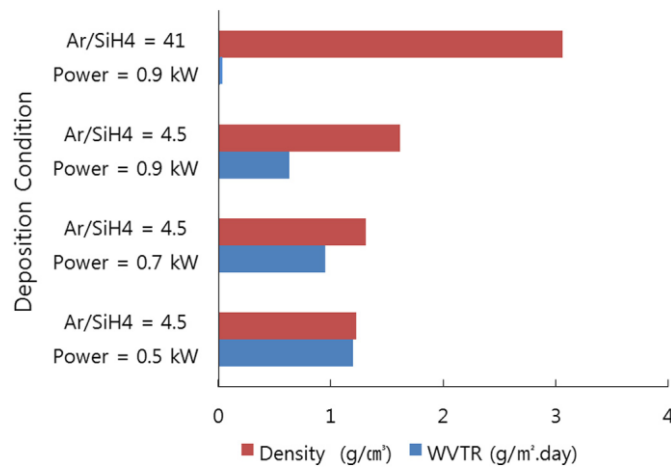


Figure 17 Effect of Ar/SiH_4 ratio and RF power variation on the density and WVTR of 100 nm-thick SiO_xN_y films deposited using $\text{O}_2/(\text{O}_2+\text{N}_2)$ ratio of 0.1.

Fig. 17 shows how the film density and WVTR varied with RF power and Ar/SiH₄ gas ratio. The film density steadily increased from 1.23 g/cm³ to 1.62 g/cm³ as the RF power increased from 0.5 kW to 0.9 kW at Ar/SiH₄ and O₂/(O₂+N₂) of 4.5 and 0.1, respectively. However, it abruptly increased to 3.06 g/cm³ at 0.9 kW when Ar/SiH₄ was increased from 4.5 to 41. This result is consistent with the abrupt decrease in the porosity in the cross-sectional morphology of the SiO_xN_y barrier film in Fig. 16(d) compared with those of Fig. 16(a)-(c).

As RF power was increased from 0.5 kW to 0.9 kW at Ar/SiH₄ and O₂/(O₂+N₂) of 4.5 and 0.1, respectively, the WVTR of SiO_xN_y films gradually decreased. However at Ar/SiH₄ of 41, the WVTR decreased drastically to 7.6×10^{-3} g/m²·day. Compared to the WVTR, 1.2 g/m²·day, of the SiO_xN_y film deposited at 0.5 kW A with r/SiH₄ of 4.5, the WVTR, 7.6×10^{-3} g/m²·day of the film deposited at 0.9 kW with Ar/SiH₄ of 41 was tremendously reduced by more than 150 times. These drastically different WVTR values would be obviously attributed to the different densities of the SiO_xN_y films shown in Fig. 17. As not shown here, the result of the sample deposited at 0.3 kW with Ar/SiH₄ and O₂/(O₂+N₂) gas ratios of 4.5 and 0.1 was 1.29 g/m²·day, which was similar to the sample deposited at 0.5 kW.

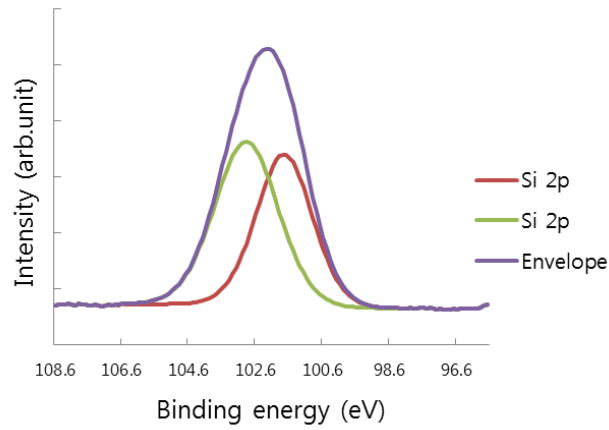


Figure 18 Si 2p core-level XPS spectra of 100 nm-thick SiO_xN_y thin film deposited at Ar/SiH₄ and O₂/(O₂+N₂) of 4.5 and 0.1, respectively, with RF power of 0.9kW

Fig. 18 shows the Si 2p core-level XPS spectrum of the 100 nm-thick SiO_xN_y film deposited at a power of 0.9kW. The Si 2p spectra was deconvoluted into two component peaks by Gaussian curve-fitting, and it was confirmed that the SiO_xN_y thin film is composed of a mixture of two peaks of 103.1eV and 101.8eV.

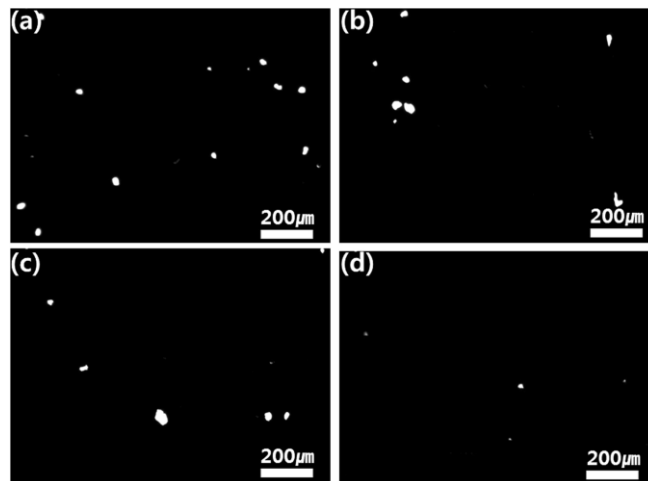


Figure 19 Ca test results of 100 nm-thick SiO_xN_y films deposited at Ar/SiH₄, O₂/(O₂+N₂) of 4.5 and 0.1, respectively with RF power of (a) 0.5 kW, (b) 0.7 kW (c)0.9 kW and (d) at Ar/SiH₄, O₂/(O₂+N₂) of 41 and 0.1, respectively, with RF power of 0.9 kW.

Fig. 19(a)-(d) shows the optical microscope (OM) images of the Ca test, which is based on the optical transmission of CaO. In this test, Ca is placed below the film. When the moisture or oxygen penetrates through the open path of the film, it will oxidize Ca, producing transparent CaO. Therefore, by observing the color changing area, the water vapor or oxygen-transmitted regions can be confirmed. As can be seen in Fig. 19(d), the SiO_xN_y film deposited at 0.9 kW with Ar/SiH₄ of 41 shows a much lower fraction of the transparent area than those of the films deposited at Ar/SiH₄ of 4.5. This Ca test result, which represents the amount of the defect areas for permeation of moisture and oxygen, is in good agreement with the WVTR data shown in Fig. 17.

As the RF power increased from 5 kW to 9 kW, the porosity decreased (Fig. 16), the density increased (Fig. 17), the WVTR data decreased (Fig. 17) and the fraction of the transparent area in the Ca test decreased (Fig. 19). As the Ar/SiH₄ ratio increased from 4.5 to 41 at the power of 9 kW, the abrupt changes in porosity, density, WVTR and the fraction of the transparent area in the Ca test were observed. The film porosity, which is revealed by the cross-section morphologies of SiO_xN_y films in Fig. 16, is consistent with the results of Figs. 17 and 18. However, it is not clearly understood why the processing conditions of the RF power and the Ar/SiH₄ ratio affect the film morphology.

It should be reminded that the substrate temperature was only 23°C. At such a low temperature, the decomposition of precursors and the atomic diffusion would be negligible on the substrate. It is expected that the decomposition of precursors would occur in the gas phase of the plasma region. If precursors are decomposed in the gas phase, the supersaturation would build up and the gas phase nucleation might occur. Ions and photo-excitations are abundant in the plasma, which are known to trigger ion-

induced and photo-induced nucleation [55, 56], respectively. In other words, there are numerous sites to trigger heterogeneous nucleation in the gas phase of the ICP-CVD process. It should be noted that the scientific community of the dusty plasma suggests that gas phase nucleation in the plasma CVD reactor is almost unavoidable under the condition of film deposition [57]. Therefore, it is possible that extensive nucleation might occur in the gas phase of the plasma region. The resultant gas phase nuclei would contribute to film deposition and be responsible for the porosity of the film. In other words, it is possible that the film should grow by non-classical crystallization[44, 58], where charged nanoparticles nucleated in the gas phase should be the building block of thin films.

In order to confirm that nanoparticles are generated in the gas phase, the carbon membrane of the Cu TEM grid were used to capture hypothetical nanoparticles for 5 s in the ICP-CVD reactor. Fig. 20(a)-(c) show STEM images of nanoparticles captured at powers of 0.5 kW, 0.7 kW and 0.9 kW with the Ar/SiH₄ and O₂/(O₂+N₂) of 4.5 and 0.1, respectively.

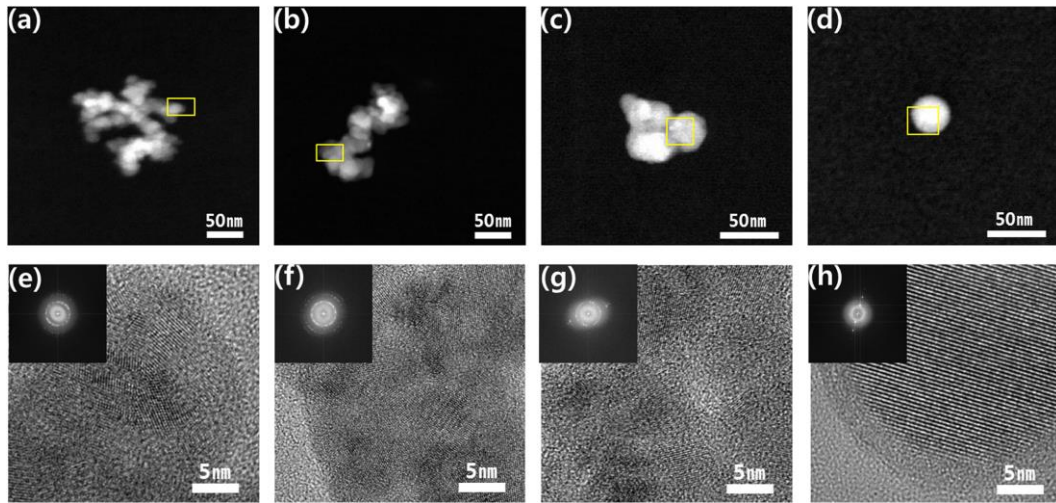


Figure 20 STEM images of primary nanoparticles captured at Ar/SiH₄ and O₂/(O₂+N₂) of 4.5 and 0.1, respectively, with RF power of (a, e) 0.5 kW, (b, f) 0.7 kW (c, g) 0.9 kW and (d, h) at Ar/SiH₄ and O₂/(O₂+N₂) of 41 and 0.1 with RF power 0.9 kW. (e), (f), (g) and (h) are magnified images respectively of the boxes in (a), (b), (c) and (d).

It was confirmed that nanoparticles were generated in the gas phase under all conditions. At 0.5 kW and 0.7 kW (Figs. 20(a) and (b)), the size of nanoparticles was in the range of 10 ~ 30 nm and the size and shape of nanoparticles were irregular. Moreover, all nanoparticles were heavily aggregated. However at 0.9 kW (Fig. 20(c)), the degree of aggregation was quite reduced compared to those of Fig. 5(a) and (b). In other words, nanoparticles tended to be less aggregated at 0.9 kW than at 0.5 kW and 0.7 kW. These results mean that the RF power in the ICP-CVD system affects the size, shape and aggregation of nanoparticles. When the Ar/SiH₄ ratio was changed from 4.5 to 41 at the fixed O₂/(O₂+N₂) ratio and power of 0.9 kW, nanoparticles were isolated without aggregation as shown by the STEM image in Fig. 20(d).

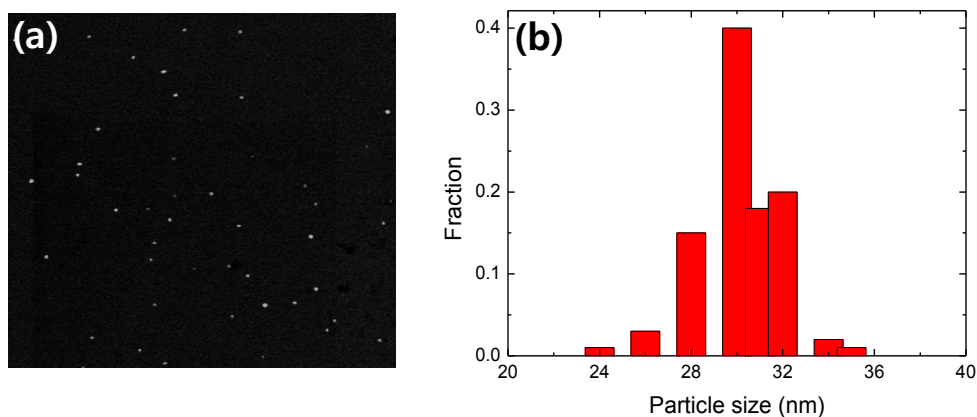


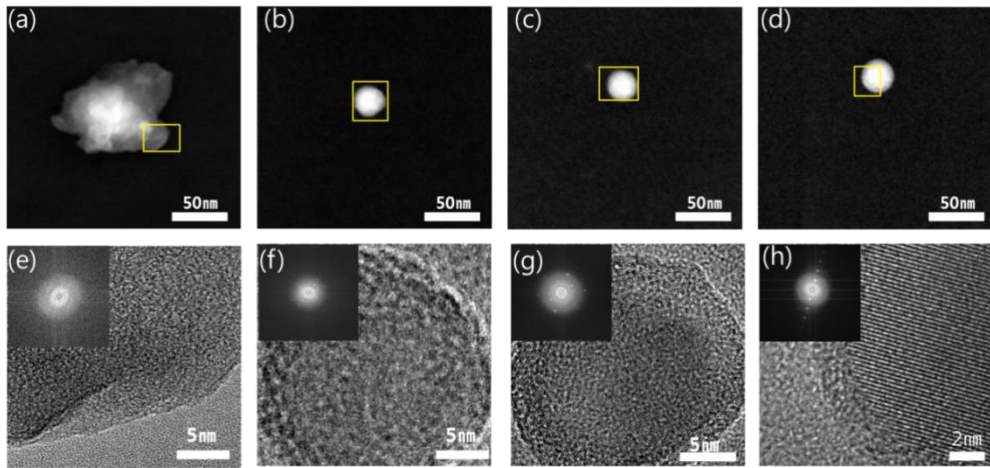
Figure 21 STEM Image and size distribution of primary nanoparticles captured at 0.9 kW with Ar/SiH₄ and O₂/(O₂+N₂) of 41 and 0.1, respectively

Besides, the shape of the nanoparticle is almost spherical. The nanoparticles were relatively mono-disperse with a size of $\sim 30 \pm 5$ nm as shown Fig. 21(a)-(b)

HR-TEM images in Fig. 20(e)-(g), which are magnified views of the boxes in Fig. 20(a)-(d), reveal that all nanoparticles have a crystalline lattice and the crystallinity of nanoparticles was further confirmed by Fast Fourier Transformation (FFT) shown in the inset of Fig. 20(e)-(g). Additionally, the lattice spacing of some nanoparticles is close to the lattice spacing of SiO₂. Considering that decomposition of SiH₄ as well as atomic diffusion is negligible on the substrate at 23°C, it would be difficult for the crystalline phase to be formed on the substrate, further indicating that crystalline nanoparticles were formed in the gas phase.

In addition, Fig. 20(h) shows that the single nanoparticle has the same lattice fringe over the entire area, indicating that it is a single crystal. The FFT image in the inset in the upper left corner of Fig. 20(h) also supported single crystallinity. The spacing between the parallel lattice fringes was measured to be 0.16 nm, which is (210) plane of

α -SiO₂, indicating that some of nanoparticles are SiO₂. Considering that the temperature of the plasma region in the ICP-CVD is not high, it is difficult to understand the formation of the crystalline phase. According to the theory of non-classical crystallization [58], charged nanoparticles have somewhat liquid-like property, which helps in their epitaxial landing and evolution into dense films. It is well established that nanoparticles formed in the plasma region are multiply charged. Combining Figs. 16 and 17 with Fig. 20, the degree of aggregation of nanoparticles in the gas phase appears to be related with the porosity and density of films: with decreasing tendency of aggregation, the porosity and density would decrease and increase, respectively. The film with minimum porosity and maximum density was obtained when there was no aggregation of nanoparticles: the dense film of Fig. 16(d) was deposited under the condition where non-aggregated single nanoparticles were generated as shown in Fig. 20(d)



25/38

Figure 22 STEM images of primary nanoparticles captured at Ar/SiH₄ and O₂/(O₂+N₂) of 41 and 0.1, respectively, with RF power of (a, e) 0.3 kW, (b, f) 0.5 kW (c, g) 0.7 kW and (d, h) 0.9 kW. (e), (f), (g) and (h) are magnified images respectively of the boxes in (a), (b), (c) and (d).

Fig. 22 shows that nanoparticles were generated in the gas phase under all conditions. Except for the nanoparticles generated at 0.3kW, nanoparticles were isolated without aggregation as shown by the STEM image in Fig. 22. The shape of nanoparticles was changing to the perfectly spherical as increasing RF Power and it is probably due to the effect of the multiple charging, which suppresses aggregation between nanoparticles.

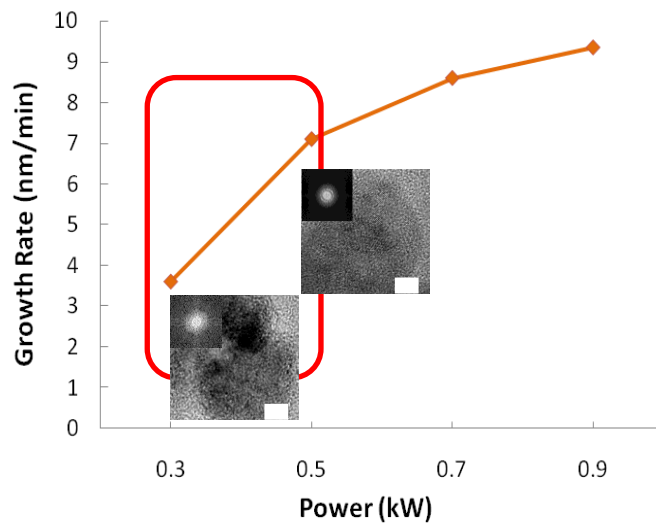


Figure 23 Behavior of Growth rate of SiO_xN_y films as a function of RF power at Ar/SiH₄ and O₂/(O₂+N₂) of 4.5 and 0.1, respectively,

Fig. 23 shows that the growth rate of SiO_xN_y films increased from 3.5nm/min to 9.4nm/min with increasing RF powers from 0.3kW to 0.9kW in ICP CVD system. Especially, a noticeable increase of the growth rate was detected between 0.3 kW to 0.5 kW and the change of crystallinity occurred from amorphous to crystal, which means that the characteristic of plasma is abruptly changed between 0.3 kW to 0.5 kW. In other words, high plasma density might be generated at a power of above 0.5 kW. In general,

high plasma density is favorable to the decomposition of precursors since many electrons collide with them. Hwang et al.'s insistence could be also supported by CLARE et al.' insistence that charges on the clusters weaken silicon-silicon and silicon-hydrogen bonds as electrons are either added to antibonding orbitals or removed from bonding orbitals [59]. For instance, when neutral SiH_4 with bond strength of 3.9 eV was negatively (SiH_4^-) or positively (SiH_4^+) charged, bond strength of the SiH_4^- and SiH_4^+ was reduced to the 0.98 eV and 0.3 eV, respectively. Thus considering this, it is plausible that nanoparticles are more likely to be multiple charged at a high plasma density region in ICP CVD reactor, which reduces the bond strength of the matters. As a result they have liquid like property, and diffusions are enhanced, which leads to the formation of crystalline SiO_xN_y nanoparticles. In other words, if nanoparticles generated in ICP CVD are charged, they could act like a quasi-solid, whose atomic diffusion was enhanced to a degree that it almost seemed like a liquid. Therefore, it is suggested that the generation of crystalline SiO_xN_y nanoparticles seemed to come from the liquid like properties of charged nanoparticles.

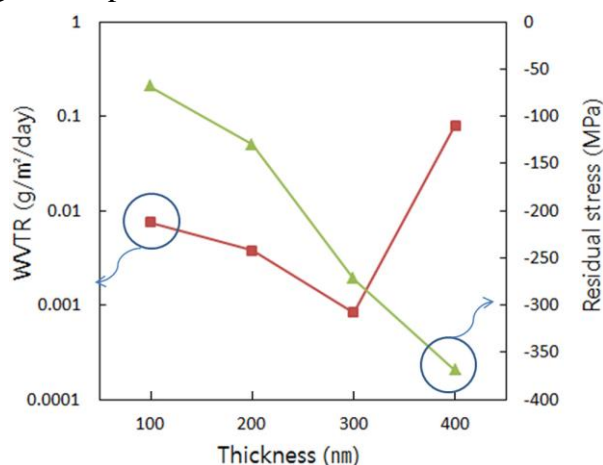


Figure 24 WVTR and residual stress of SiO_xN_y films deposited at Ar/SiH_4 and $\text{O}_2/(\text{O}_2+\text{N}_2)$ of 41 and 0.1, respectively, with RF power of 0.9 kW as a function of film thickness.

To optimize the barrier property, SiO_xN_y films were deposited at different film thicknesses on the PET substrate under the best condition of 0.9 kW with Ar/SiH₄ and O₂/(O₂+N₂) ratios of 41 and 0.1, respectively. Their WVTR and residual stress were measured as shown in Fig. 20. The residual stress gradually increased from -68 MPa to -369 MPa when the SiO_xN_y film thickness increased from 100 nm to 400 nm. The minus sign means that films are in the compressive residual stress. In particular the 400 nm-thick SiO_xN_y film showed the highest compressive stress of -369 MPa. Similarly, the WVTR values steadily decreased from 7.6×10^{-3} to 8.4×10^{-4} g/m²·day with increasing film thicknesses up to 300 nm. However, the WVTR value was drastically degraded to 8.0×10^{-2} g/m²·day at the 400 nm-thick film. This means that the increase of the SiO_xN_y film thickness increases the residual stress, which could generate some defects such as micro-cracks.

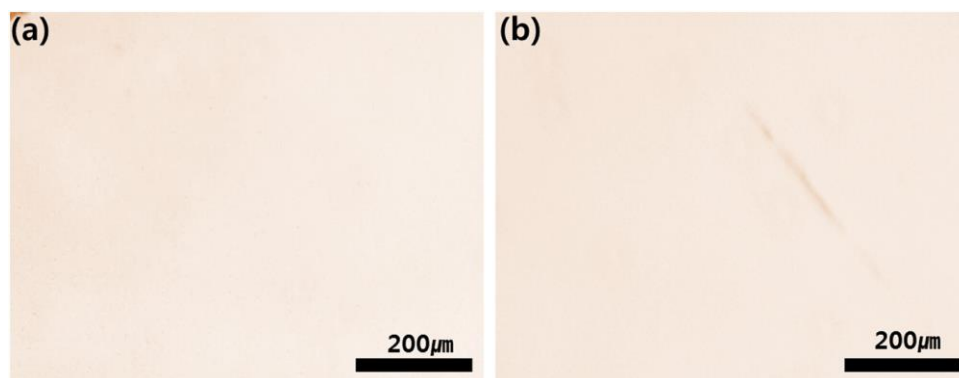


Figure 250M images of (a) 300 nm-thick SiO_xN_y film, (b) 400 nm-thick SiO_xN_y film deposited at Ar/SiH₄ and O₂/(O₂+N₂) of 41 and 0.1, respectively, with RF power of 0.9 kW.

To confirm this possibility, the surface of the films was examined by an optical microscope (OM). The OM images of the SiO_xN_y films deposited on PET substrates are shown in Fig. 7. The SiO_xN_y film with a thickness of 300 nm shows a clean surface image whereas the film with a thickness of 400 nm shows some micro-cracks. Therefore, the severe degradation of the WVTR values at 400 nm would be attributed to such micro-cracks, which would be caused by the increased residual stress.

4. Conclusion

The aggregation and crystallinity of nanoparticles were greatly affected by RF power and the Ar/SiH₄ ratio. Isolated nanoparticles of a spherical shape without any aggregation were generated in the gas phase at high power of 0.9 kW with high Ar/SiH₄ ratio of 41, which leads to the high film density and outstanding barrier property. In contrast, heavily aggregated nanoparticles of an irregular shape were generated in the gas phase at low power of 0.7kW with low Ar/SiH₄ ratio of 4.5, which leads to porous encapsulation layers, where and poor barrier property. The barrier property was also affected by the residual stress with increasing film thickness.

Ch. 3 Permeation barrier properties of silicon oxide films deposited on Polyethyleneterephthalate(PET) substrate using roll-to-roll reactive magnetron sputtering system

1. Introduction

The use of plastic substrates allows for many new applications in the field of flexible optoelectronic devices such as organic light-emitting diodes (OLEDs), organic photovoltaics (OPVs), and organic solar cell [3, 7, 21, 25]. Especially, OLEDs are considerably attractive for display due to their inherent advantages of wide viewing angle, fast response time, high brightness, and low power consumption [3, 4, 60]. However, the long-term stability of flexible OLEDs is limited due to the instability of the organic materials and low work function metals by the permeation of moisture and oxygen into the plastic substrates which, unlike glass, have poor barrier properties [61-63]. This can lead to severe deterioration of their performance and reduces lifetime. Therefore, barrier layers are absolutely indispensable to protect OLEDs from moisture and oxygen before the great potential of OLEDs can be realized [63]. In order to ensure a long lifetime for flexible OLEDs device, water vapor transmission rate (WVTR) must be less than 10^{-6} g/m²/day. Generally, two ways are considered to get the required property. One is the optimization of barrier layers grown by atomic layer deposition (ALD) which has almost defect-free [4, 25, 26, 53]. The other approach is a combination of inorganic and organic multi-laminated layers deposited by sputtering and chemical vapor deposition (CVD). Inorganic materials such as SiO_x [7, 62, 64],

SiN_x [7, 25], SiO_xN_y [16, 65], AlO_x [26, 27, 29, 31, 64], ZrO_x [26], MgO [3, 4], TiO_x [31, 64], HfO_x [29] which have high intrinsic impermeability are often used as diffusion barrier layers, while the organic layer functions as smoothing surface for the next barrier film, interrupting growth of defect, reducing mechanical stress, and lengthening the path of diffusion [64, 66]. Although a perfect thin film encapsulation technique has not been developed so far, the above-mentioned of two approaches, the latter is more advantageous than the former given the economics. Reactive roll-to-roll magnetron sputtering is a low temperature deposition technique which can be used for attaining high quality oxide thin films. And also, this method has many other advantages including low cost manufacturing, easily controlled deposition process, and scalability to large area deposition with uniformity for various industrial application [67]. However, in the case of ALD process, practical application is expected to take some time due to the extremely low deposition rate about 1 – 3 Å/cycle and limited materials that can be deposited.

The main objective of this study is to develop the single layer of SiO_x films with superior WVTR and high transmittance properties by optimizing process condition with roll-to-roll reactive magnetron sputtering system, which can be applicable to the formation of multilayer barrier structures with organic materials. To achieve this goal, chemical composition, surface roughness, density, residual stress, water vapor transmission rate were analyzed by means of X-ray photoelectron spectroscopy (XPS), atomic force microscopy (AFM), Rutherford backscattering spectrometry (RBS), laser profile meter. Detailed observation of the barrier films were carried out by high-resolution transmission electron microscopy (HR-TEM).

2. Experimental procedure

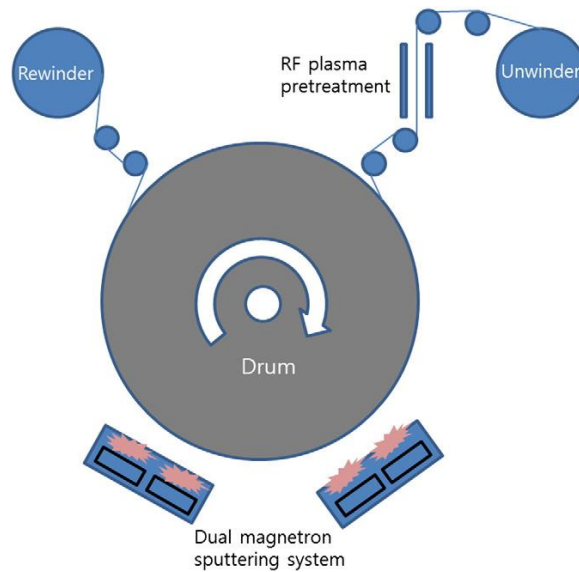


Figure 26 Schematic diagram of the roll to roll dual magnetron sputtering system to deposit the SiO_x films.

SiO_x barrier films were deposited on polyethylene terephthalate (PET) substrate (Kimoto Tech. Inc.) with a thickness of 50μm using roll-to-roll vacuum coater system. The machines can handle with a width of up to 300 mm and the web speed is variable between 0.1 and 10m/min. This chamber consists of two process chambers which are pumped separately. One is for radio frequency (RF) of 13.56 MHz plasma treatment of substrate and the other is for reactive dual magnetron sputtering of SiO_x. Before deposition of SiO_x film, plasma treatment of the PET substrate was conducted to remove any debris existed on surface and to activate the surface under 0.05kW of power generated by RF (Optimized condition in our experiment). O₂ gas with 50% Ar content was supplied at a flow rate of 100 standard cubic centimeter per minute (sccm) controlled by a mass flow controller (MFC). The rolling speed and the sputtering power

of sputtering systems were changed from 0.1 to 2.0 m/min and from 3 kW to 7 kW, respectively to control film thickness. The base pressure and working pressure during plasma treatment were 1×10^{-6} Torr and 3.8×10^{-2} Torr, respectively. After plasma treatment, SiO_x films were deposited by the reactive dual magnetron sputtering. The target size per magnetron is 320 x 124 mm². Working pressure and sputtering power were 3.2×10^{-3} Torr and 3.0-7.0kW, respectively and O₂/(Ar+O₂) gas flow ratio is 5-50 %. SiO_x films with thickness values of 100, 150, 300, and 500nm were deposited and thickness was measured using Alpha-Step[®] (ASIQ3) system after averaging at least five measurements. The root-mean-square surface roughness (Rq) and surface morphologies of the SiO_x films were measured by non-contact mode AFM (X-100, Park System). The surface density of the barrier films was examined by RBS with a beam of He⁺² particles with average energy of 2.0 MeV. The chemical compositions were characterized by XPS (Thermo VG, Scientific, SIGMA PROBE) with in situ Ar sputtering cleaning right before XPS analysis and concentrations of the Si and O were calculated from the area of the Si 2p and O 1s peaks after Shirley background subtraction. The residual film stress was assessed by the beam bending method using a thin film stress measurement instrument (FLX-2320, Tencor), and derived from the stoney formula. The measurement of WVTR was executed on a 10 cm²sample area at 35 °C and 90% relative humidity using deltaperm, Technolox. The transmittance was observed using UV/Vis spectrometer (Cary 100, Agilent technologies). Detailed observation of barrier films was carried out by HR- TEM (JEM ARM 200F, JEOL). The specimens for TEM were fabricated using an ultra-microtome.

3. Results and Discussion

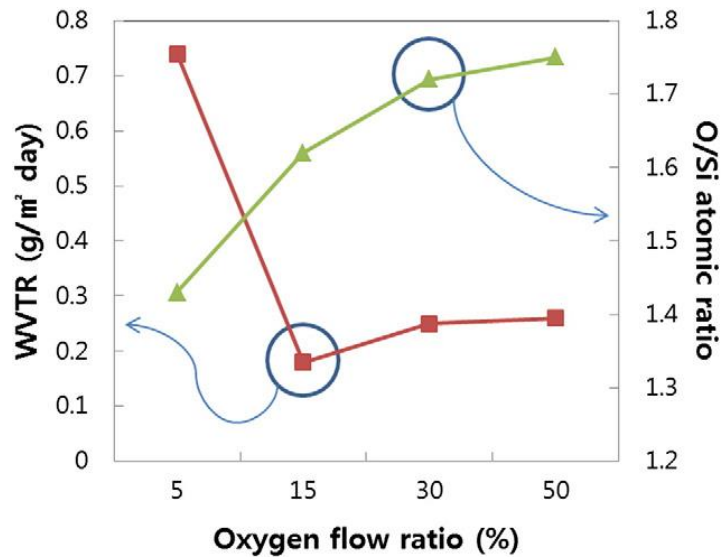


Figure 27 Change in the WVTR and O/Si atomic ratio of the 100 nm-thick SiO_x barrier films deposited on 50 μm-thick PET substrate as a function of O₂ flow ratio.

Fig. 27 shows the WVTR the O/Si ratio of 100 nm-thick SiO_x films deposited on PET substrate at the power of 3.0 kW as a function of oxygen flow ratio. The O/Si ratio which was corrected by a reference sample, thermal SiO₂ increases with increasing oxygen flow ratio. This is attributed to the fact that many oxygen ions are generated and contribute to reaction. In addition, smaller amount of argon ions are generated due to the higher partial pressure of oxygen, which reduce the sputtered silicon atoms. These two results lead to high O/Si ratio [68, 69]. The WVTR of the SiO_x films with the thickness of 100nm reaches the minimum value of $2.1 \times 10^{-1} \text{g/m}^2/\text{day}$ at 15% oxygen flow ratio and almost saturated above 15%. However, WVTR of the SiO_x films with the thickness of 100nm deposited at 5% oxygen flow ratio is $7.5 \times 10^{-1} \text{g/m}^2/\text{day}$. This difference is probably caused by the depletion of oxygen, which offers more unstable bonds at silicon atoms and brings about an increase of penetration of water molecules.

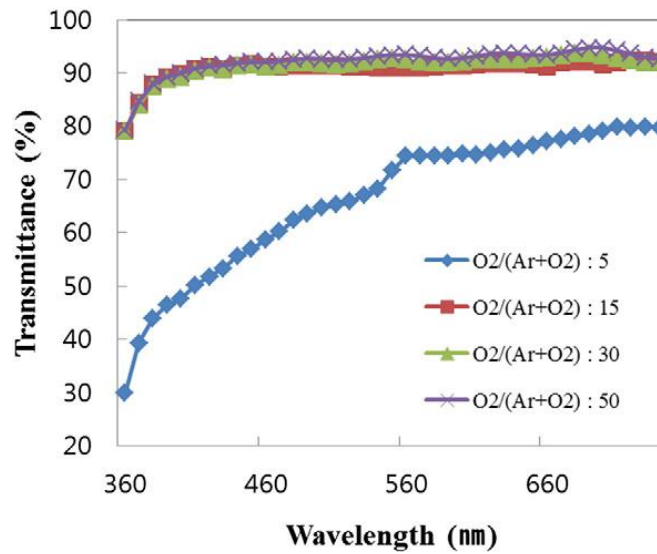


Figure 28 Optical transmittance of 100 nm - thick SiO_x films prepared by reactive sputtering according to O₂ content.

The optical transmittance as a function of oxygen content is presented in Fig. 28. When the oxygen content was 5%, the transmittance at 550 nm was about 67% showing a brown thin film. This is because of the residual silicon atoms in the film which didn't react with oxygen. However, Optical transmittance at 550 nm was over 90% when the oxygen content was over 15%, even similar raw PET.

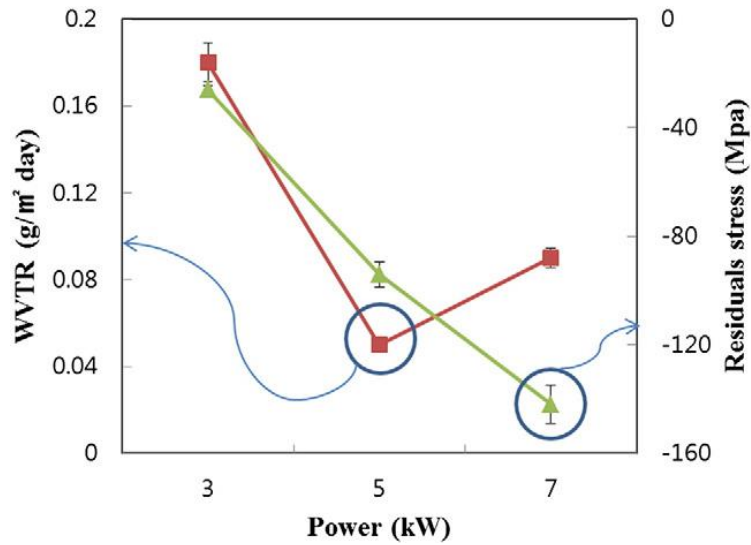


Figure 29 Change in the WVTR and residual stress of 100 nm-thick SiOx films deposited on 50 μm -thick PET substrate as a function of sputtering power.

Fig. 29 illustrates the WVTR and residual stress of SiOx films with a thickness of 100 nm as a function of the sputtering power. As a sputtering power increases from 3.0 to 5.0 kW, the WVTR value abruptly decreases from 1.85×10^{-1} to 5.62×10^{-2} g/m²/day, but increase to 8.4×10^{-2} g/m²/day again at the power of 7.0 kW. This is because high sputtering power can deposit denser films, and has better performance to prevent the permeation of water vapor. However, much higher sputtering power can induce some defects at nanometer scale in the film, and hence cause an increase of WVTR property. Leterrier et al. Reported that sparsely distributed large defects and nano-scale defects were main pathways of the water vapor in the films [70] and this result is similar with that reported by Lin et al [68]. In terms of the residual stress, it increases from -26 to -102 MPa with increasing sputtering power. The minus sign means that films are in the compressive state. This compressive stress can be explained by the implantation of extra

atoms in the film during deposition or the micro deformations related with energetic atomic collisions [71]. The additional atoms stretch the material near surface, which causes to compressive stress due to the constraint of the underlying film. Moreover, energetic atomic collisions with surface of the film result in a film deformation [71]. For free standing or unrestricted material, there would be little stress. However, in this case, compressive residual stress is generated since SiO_x film is attached to a PET substrate. The residual stress of this SiO_x film is the results from the following two aspects: thermal stress and growth-induced stress [72]. The thermal stress is an extrinsic stress due to the difference in coefficient of thermal expansion (CTE) between the PET substrate and the SiO_x film. Therefore, the shrinkage of the SiO_x films differs from that of the PET substrate during deposition process. The growth-induced stress is intrinsic stress resulted from the ion bombardment during the growth of the film. In the case of our system, we think that the growth-induced stress is a dominant factor for an increase of residual stress due to an increase of ion bombardment effect since kinetic energy of the impinging ions increases with increasing sputtering power. From these results, we considered that the difference in the WVTR value of the SiO_x films deposited at 5.0 to 7.0 kW is not due to the residual stress, but probably due to other effects such as the change of the surface morphology or density of the films. To confirm this postulation, the surface roughness and density of the films were investigated by AFM and RBS.

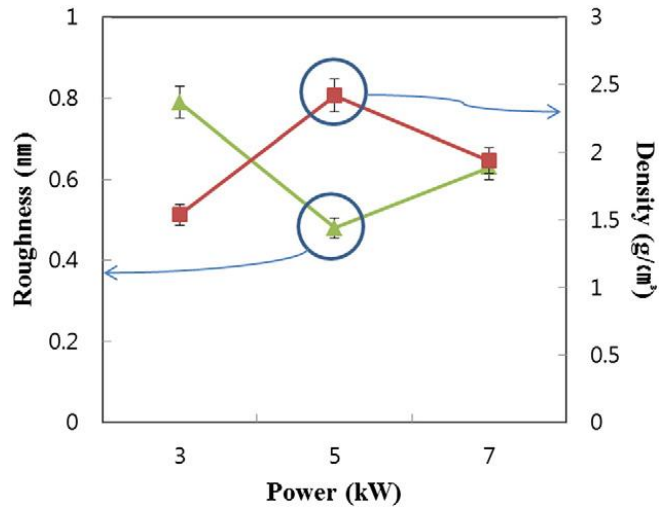


Figure 30 Surface roughness and density of 100 nm-thick SiOx films fabricated using various sputter power.

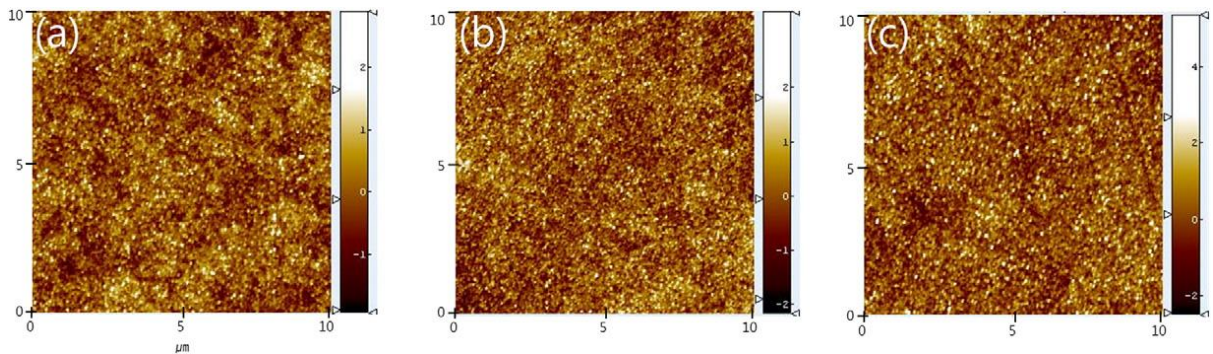


Figure 31 AFM image showing the surface roughness of 100 nm-thick SiOx films deposited as a function of sputtering power (a) 3.0 kW, (b) 5.0 kW, (c) 7.0 kW.

As seen in Fig. 30-31, the surface roughness and density of 100 nm- thick SiOx films were different as a function of sputtering power. The surface roughness of films deposited at the power of 3.0 and 5.0 kW was 0.79 and 0.48nm, respectively. However,

when sputtering power was further increased at 7.0 kW, it increased to 0.63 nm. This can be explained by the conflict contribution of deposition rate and the energy of sputtered atoms impinged on substrate. An increase of sputtering power causes rises of flux of the sputtered atoms to the substrate and gives more energy to the particles impinging on the substrate, which makes it diffuse more easily within the growing films [73]. Although sputtered atoms on the substrate at high sputtering power have short period to move their stable site, enough high energy of the particles assists their migration on surface so that surface roughness appeared lower when the sputtering power was increased [74].

However, when the sputtering power was excessively increased, surface roughness adversely increased due to the side effect of ion bombardment to the films. In contrast to the surface roughness, an increase of the film density with sputtering power can be observed. The density of films deposited at the power of 3.0 and 5.0 kW was 1.54 and 2.42 g/cm³, respectively. However, when the sputtering power was further increased at 7.0 kW, it reduced to 1.94 g/cm³. This behavior is also due to the effect of ion bombardment as mentioned above. An increased ion bombardment leads to rearrangement of atoms during the film growth since surface diffusion was enhanced, and hence lead void diminution, which results in silicon oxide network densification [75]. However, if the input power further increases at 7 kW, the density quality of SiO_x films becomes poor as 1.94 g/cm³. This is because of surface damages by high energetic atoms. These observations indicate that sputtering power up to 5 kW plays substantial role in determining smoother surface roughness and enhanced density of the films, which is favorable for improved WVTR properties.

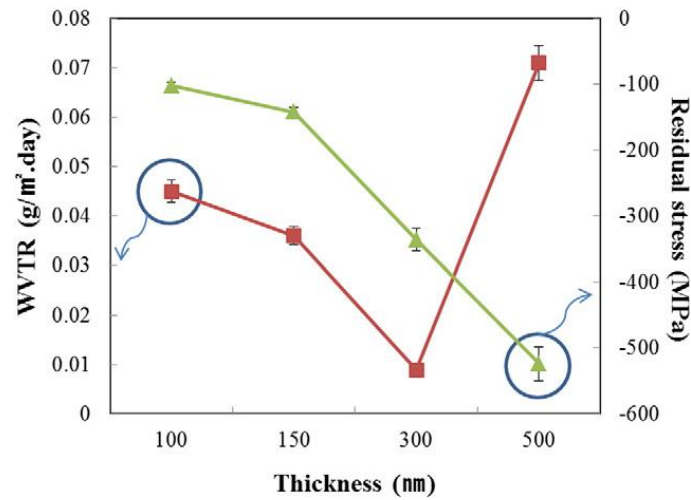


Figure 32 Change in the WVTR and residual stress of the barrier films deposited on 50um – thick PET substrate as a function of film thickness.

Fig. 32 shows the WVTR and residual stress as a function of SiOx film thicknesses coated on the PET substrate. As shown in Fig.32, the residual compressive stress of SiOx films gradually increased from -102 to -524 MPa as the SiOx film thickness increased from 100 nm to 500nm, and especially the 500 nm-thick SiOx film showed the highest compressive stress value of -524MPa. The WVTR initially decreased with increasing the film thickness and reached to $8.9 \times 10^{-3} \text{ g/m}^2/\text{day}$ for the PET substrate coated with a 300 nm-thick SiOx, which showed outstanding WVTR value. This result shows 25 to 300 times less WVTR values compared to the other reports. For instance, Lau et al. showed WVTR value of $114 \times 10^{-2} \text{ g/m}^2/\text{day}$ [16]and Kim et al. presented the WVTR value of $3.1 \times 10^{-2} \text{ g/m}^2/\text{day}$ with a multilayered structure of SiOxNy/Ag/SiOxNy deposited by sputtering [65, 76]. Furthermore, Fahlteich et al. prepared inorganic materials such SiO₂, AlO₂, ZnSn_xO_y, ZnO and TiO₂ using sputtering and exhibited the WVTR value of 1.5×10^{-2} , 3.0×10^{-2} , 1.0×10^{-2} , 3.0×10^{-2} , and $3.0 \times 10^{-1} \text{ g/m}^2/\text{day}$, respectively [61, 64]. Moreover, the WVTR value of 1.1×10^{-2} was

obtained from the structure of Al₂O₃/Ag/ Al₂O₃ deposited by jeong et al. research group [17, 77]. However, as the SiO_x film thickness reached 500 nm, the permeability was obviously degraded to $7.1 \times 10^{-2} \text{g/m}^2/\text{day}$ higher than that of the 300 nm-thick SiO_x film, indicating that much thicker SiO_x film would not consequently cause the decreasing WVTR. The higher residual stress in a certain range of film thickness, which blocks off many defect and increases the tortuosity of the pathways is beneficial to the barrier performances[78, 79]. However, much higher compressive stress can also lead to appearance of the defects such as micro-crack, which results in an increase of the permeation of water vapor. These results imply that the WVTR value of the SiO_x films could be further optimized by controlling the residual stress with the adequate thickness of SiO_x films. In this study, low WVTR value of $8.9 \times 10^{-3} \text{g/m}^2/\text{day}$ was obtained from the 300 nm-thick SiO_x film with compressive stress of -336MPa.

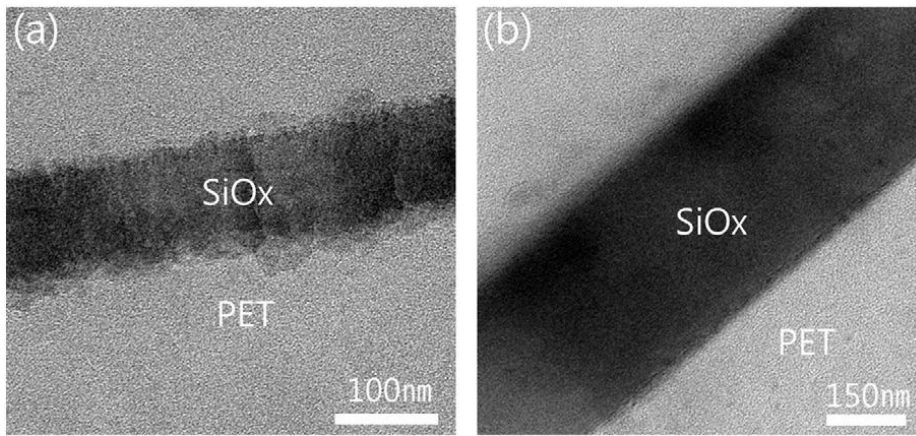


Figure 33 TEM micrograph of the SiO_x films deposited on PET substrates using (a) 5% O₂/95% Ar at the power of 3.0 kW and (b) 15% O₂/85% Ar at the power of 5.0 kW.

Fig. 33a and b show HR-TEM images of the 100 nm-thick SiO_x film deposited at the power of 3.0 kW in 5 % O₂/ 95 % Ar and the 300 nm-thick SiO_x film deposited at

the power of 5.0 kW in 15 % O₂/85 % Ar, respectively. The upper side is the SiO_x layer, and the lower side is the PET substrate. Both films have no detectable grain boundaries. This means that the SiO_x films deposited by reactive sputtering deposition possess amorphous structure. In addition, an apparent difference was observed at the interface between the PET substrate and SiO_x layers. The interface of SiO_x/PET films deposited at the power of 3 kW in 5 % O₂/ 95 % Ar is very rough and not uniform. However, we detected little micro-defect inside of the SiO_x films and observed very smooth and uniform SiO_x/PET interface of the film deposited at the power of 5 kW in 15 % O₂/85 % Ar. As seen Fig.32, we obtained low WVTR value of 8.9×10^{-3} g/m²/day with the residual stress value of -336 MPa. Generally, high residual stress of the film is beneficial to the barrier properties. However, it does not help to enhance the bending performance when we consider this barrier film for application of flexible display in industry. Hence, the development of barrier films which have excellent barrier properties with low residual stress is really important.

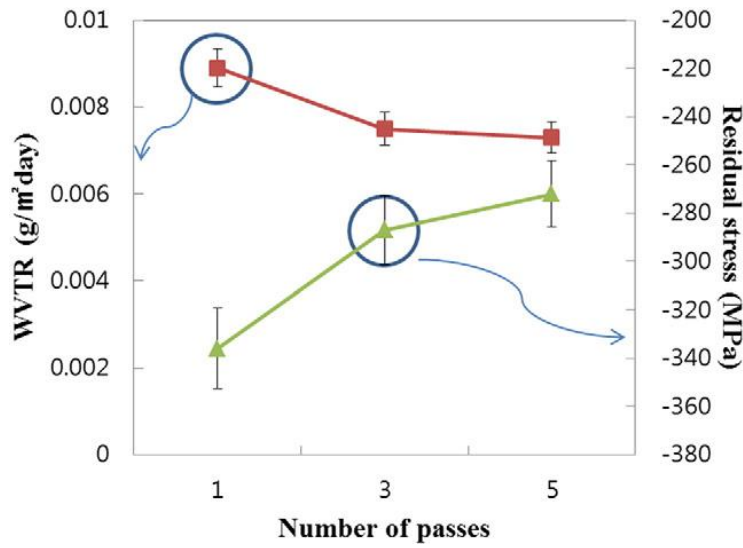


Figure 34 Change in the WVTR and residual stress of the SiOx barrier film as a function of the number of passes of web at constant total film thickness with 300 nm.

The residual stress and WVTR property of the SiOx barrier film are shown in Fig. 34 as a function of the number of the passes of the web at constant total film thickness with 300 nm. It is clearly shown that the residual stress considerably decreased from -336 Mpa to -272Mpa with increasing passing numbers. In addition, the WVTR property was slightly more enhanced from $8.9 \times 10^{-3} \text{ g/m}^2/\text{day}$ to $7.3 \times 10^{-3} \text{ g/m}^2/\text{day}$, which shows outstanding WVTR property. To the author knowledge, this very low barrier property for a single layer of SiOx film has never been achieved from sputtering technology. These results allow us to conclude that multiple passes play an important role in reducing residual stress and improving the WVTR property. This is because it is possible that multiple passes more effectively hinder many defects which existed in the previous passes by decoupling than that of the single passed barrier film. It is expected that this low residual stress barrier film with superior barrier property would help to

increase the reliability for the flexible display in industry. However, detailed analysis about how the process of multiple passes contributes to lower residual stress and improved WVTR is required. Overall, it is found that the characteristics of low surface roughness, high packing density, uniform interface of SiO_x/PET, and deposition of multiple pass may all contribute to the enhanced barrier performance.

4. Conclusions

In this study, reactively sputtered SiO_x films were developed and characterized. The SiO_x films were deposited on the PET substrate in O₂ plasma. Details of the SiO_x properties in terms of the residual stress, surface roughness, density, interfaces were investigated as a function of sputtering power and film thickness. Even though the SiO_x films seem to become much denser, smoother with increasing the sputtering power, the higher sputtering power caused the barrier performance to fail by making film surface rough and less dense. An enhancement of the WVTR value was also observed for a rise in the thickness of SiO_x films. The high transparency of 91 % and superior WVTR value of 7.7×10^{-3} g/m²/day were obtained at the 300 nm-thick SiO_x films as a single layer, which might be mainly because of an increase of tortuosity of the pathway. In addition, residual stress of the barrier film with excellent barrier property was reduced by using multiple passing techniques. However, an increase above 300 nm resulted in a degradation of the permeation property. Overall, the density, surface roughness, and residual stress of the films are controlled by the sputtering power. When we consider

process economies and applications in industry, it is necessary to deposit the barrier films as thin as possible.

Ch. 4 Independent Topics

Improvement of NiMoNb to polyimide adhesion by inductively coupled nitrogen plasma treatment

1. Introduction

Flexible printed circuit boards (FPCBs) have stimulated the attention of researchers due to various industrial applications such as cellular phones, smart cards, energy panels, cameras, computers, flexible display modules, and are expected to be used more in upcoming flexible IT electronics [80, 81]. Especially, since electronic devices become smaller and lighter, there are tremendous needs to replace the conventional rigid circuit board with flexible polymer substrates. FPCBs have many advantages compared to a rigid circuit board, because of its flexibility, especially in applications demanding more integrated electronic devices, and can be mass produced using the roll-to-roll manufacturing system [82]. Polyimide (PI) has the desirable properties of low dielectric constants, good dimensional stability, high temperature resistance, high chemical stability, good mechanical strength, and hence it has been used as a flexible substrate in electronic devices [83-85]. Flexible copper clad laminate (FCCL) is generally employed as a raw material for FPCBs. Compared to the casting or laminating type of FCCL, sputtered FCCL has many advantages such as its fine pitch etching and dimensional accuracy as the device dimensions are scaled down [86]. In addition to the lithography process to make fine pitch, many techniques such as inkjet printing, laser-induced forward transfer (LIFT) have also been studied. Especially, LIFT is one of the attractive technique because it allows working various viscosities (1-10³mPas), obtaining high degree of spatial resolution compared to the inkjet printing

which has problem of nozzle contamination or clogging. However, despite of these advantages there are still some problems like splatter and short length of the printed lines which limit its industrial implementation [87-89]. Due to the extremely poor interfacial adhesion of Cu on the PI substrate, it is difficult to further decrease the width of the metal lines. It causes the failure of the FCCL because of the huge stress concentration at the interface between the Cu and the PI substrate upon bending, twisting, and stretching [84]. Therefore, poor adhesion of Cu to PI has to be overcome to enhance the reliability and flexibility of FCCL. A number of studies have been investigated on the adhesion properties. An addition of adhesion layers between the Cu and PI substrate using CuCr [90], CuTi [91] Ni [92], NiCr [82, 83, 93-95], Cr [84, 96-98], , NiMoNb [99], indium tin oxide (ITO) [92, 100] has been reported to improve adhesion. Moreover, the control of PI surface by various surface treatment such as ion beams [93, 101-103], plasma [92, 95, 104-108], and chemical solution [109], which induces either mechanical, chemical or physical changes has been also suggested to enhance peel strength. However, knowledge of the adhesion properties of Cu/NiMoNb/polyimide system remains still insufficient. The aim of this research is to develop a NiMoNb adhesion films with outstanding peel strength, especially after annealing treatment, using inductively coupled plasma (ICP) treatment of PI. To attain this goal, film density, chemical composition, chemical binding state, peel strength, and Cu/NiMoNb/PI interface were analyzed by means of Rutherford backscattering spectrometry (RBS), X-ray photoelectron spectroscopy (XPS), peel test, and high-resolution transmission electron microscopy (HR-TEM).

2. Experimental procedure

The FCCL structures investigated in this research was Cu/NiMoNb/PI. The substrate material was 25 μm -thick PI film (SKC, Korea). The plasma treatment of the PI substrate was conducted under 0.2 kW and 0.9kW of power generated by internal type of ICP system.

The ICP was generated in the region between the gas distributor and the substrate by applying 13.56 MHz power through a tuning network to a one-turn coil (RFI coil) of a water-cooled copper tube. The RFI coil had a diameter of about 100 mm and it was located inside of the vacuum chamber. Nitrogen (N_2) gas with 90 % argon (Ar) content was supplied at a flow rate of 35 standard cubic centimeter per minute (sccm) controlled by a mass flow controller (MFC). ICP plasma treatment was performed at room temperature. The base pressure and the working pressure were 8.7×10^{-7} Torr and 6.2×10^{-3} Torr, respectively. Firstly, ICP plasma treatment was performed on the PI substrate, and secondly 20 nm-thick NiMoNb and 60 nm-thick Cu films were deposited in the DC magnetron sputtering system. The ratio of the NiMoNb target was 85.0:12.3:2.7. The NiMoNb sputtering power ranged from 0.2 kW to 0.8kW, and the flow rate of the Ar gas was 200 sccm. The pressure maintained during sputtering was 3 mtorr. After sputtering of NiMoNb and Cu, the samples were subsequently electroplated to a thickness of 12 μm . A peel angle of 180° was used for 10 peel test specimens. The dimensions of samples were 100-mm long and 1-mm wide, which were patterned by wet etching. The peel test results of the samples exhibiting the minimum and maximum values were removed to measure the average peel strength. In order to evaluate the thermal reliability of the FCCL, we measured the peel strength of the as-deposited and

annealed FCCL samples. In particular, thermal annealing was carried out in an oven at 150°C for 24 h. The density of NiMoNb layers was analyzed by RBS and surface roughness was measured by Atomic force microscopy (AFM, X-100, Park Systems.). The chemical bonding state of the PI substrate in the fractured films after the peel-off test was characterized by XPS (Thermo VG Scientific, SIGMA RPOVE). The state of the interface regions was examined by HR- TEM using a JEOL 3010F instrument operated at 300 kV. The specimens used for TEM were fabricated using a dual-beam focused ion beam (FIB) (Helios Nano-LabTM, FEI). Subsequently, the surface regions damaged by FIB milling were eliminated using a low-energy ion-milling system (GentleMillTM3 system, model IV8) at 0.7 kV and ~10° beam incidence [28].

3. Results and Discussion

3.1. Peel strength

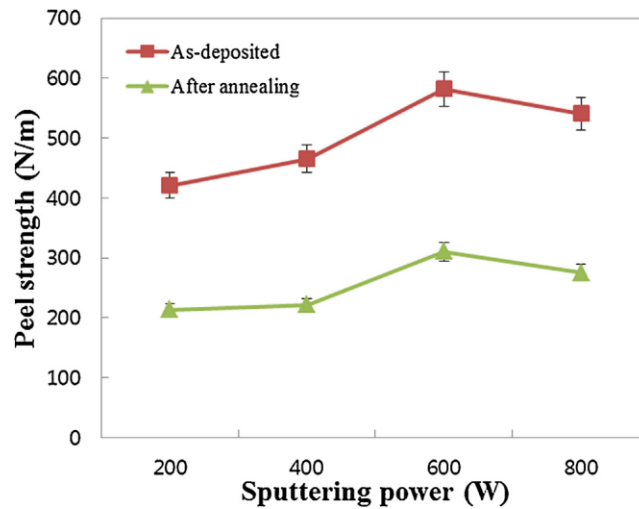


Figure 35 Peel strength of the FCCLs according to the sputtering powers of the NiMoNb adhesion layers.

Fig. 35 shows the value of peel strengths for the as-deposited and thermally annealed FCCL structures with 20 nm-thick NiMoNb adhesion layers deposited on raw PI substrate as a function of sputtering power. The peel strengths in the as-deposited and annealed FCCL were 421~582 N/m and 213-310 N/m, respectively. As the sputtering powers increased, the peel strength in the as-deposited and annealed FCCL were gradually enhanced up to at the sputtering power of 600 W, but decreased at the sputtering power of 800W. The difference in the peel strength between the films deposited at the power of 200 W and 600 W was probably due to an increase of effect of the ion bombardment. An increase of sputtering powers causes rises of flux of the sputtered atoms to the PI substrate and gives more energy to the particles, which improve migration of atoms on the surface. However, when the sputtering power further increased, the value of peel strength was degraded by the excessive effect of ion bombardment.

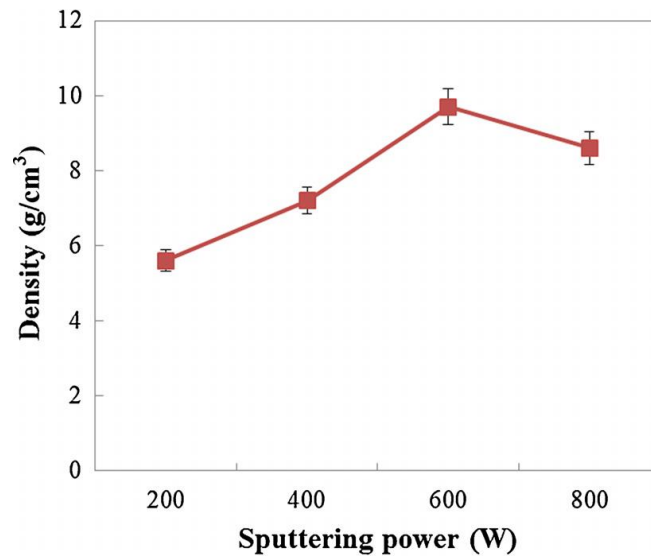


Figure 36 Density of NiMoNb adhesion films according to the sputtering power.

Fig. 36 shows the value of film density as a function of sputtering power. The film density steadily increased from 5.6 g/cm³ to 9.7 g/cm³ up to the power of 600 W, however it decreased to 8.6 g/cm³ at the power of 800 W. These results imply that there is significantly correlated between the peel strength and film density.

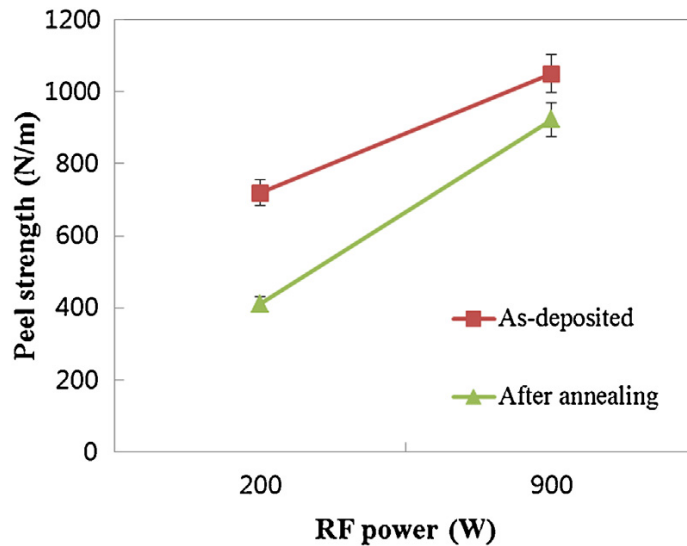


Figure 37 Peel strength of the FCCLs treated plasma as a function of RF power before NiMoNb deposition.

Fig. 37 shows the peel strength of the as-deposited and annealed FCCL which was treated ICP plasma before deposition of NiMoNb adhesion layers. There are dramatic increases of the peel strength compared to the FCCL without ICP plasma treatment. The peel strengths in the as-deposited and annealed FCCL were 720~1050 N/m and 364~923 N/m, respectively, which is outstanding peel strength. Especially, the value of peel strengths obtained from the annealed FCCL in this study (923N/m) was much higher than that of previously reported researches. For example, Miyauchi et al. presented the value of peel strength of 620 N/m in the annealed FCCL with NiCr adhesion layer[107]. In addition, the peel strength values of 686 N/m and 323 N/m in the as-deposited and annealed FCCL having a NiCrX (X= refractory materials) were

obtained by Park et al. research group [110]. Moreover, The FCCL with a Cr adhesion layer subjected to aging at 130 °C for 168 h exhibited the peel strength of 324 N/m[111]. The substantial increase of the peel strength of ICP plasma-treated FCCLs might be explained by the postulation that the plasma treatment of PI substrates can modify the morphology and chemical molecular structure on the PI substrate, which provides more nucleation site, and hence leads more chemical reaction of NiMoNb with plasma-induced functionalities. To confirm this assumption, the surface roughness, chemical binding state were analyzed by, AFM, and XPS.

3.2 Surface roughness of PI films

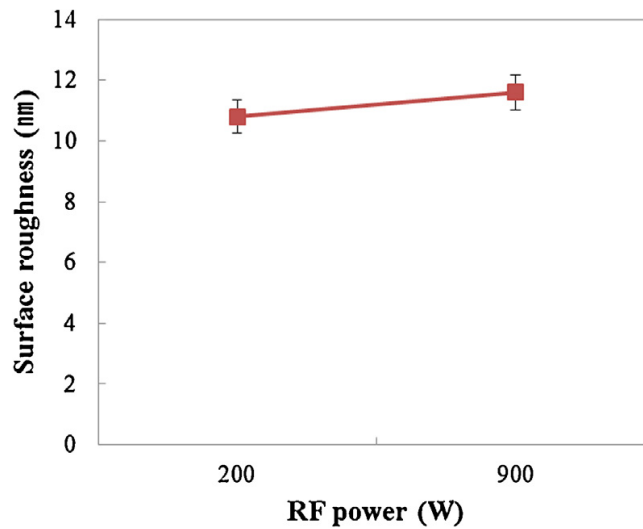


Figure 38 Relationship between the surface roughness and RF power.

As shown Fig. 38, the RMS surface roughness between 200 W and 900 W of the ICP power-treated PI substrates was 10.9 and 11.5 nm, respectively, which means that the RMS roughness of the PI surfaces was not significantly affected by these two plasma conditions, probably due to long distance between the PI substrate and RFI Coil, approximately 15 cm. Generally, the peel strength between a PI and a metal has been

mainly affected by the change of the surface roughness and chemical modification of the polymer surface. Noh et al. reported that plasma treatment of the substrate could increase the surface area and change chemical functional groups of the PI substrate, which improves the mechanical interlocking and chemical bonding between the PI and metals [82]. However, excessive plasma treatment could result in chain scission, and hence lead to a weak boundary layer which degrades the peel strength of the FCCL. In general, increase of the surface roughness and chemical functional groups on the PI surface have a great effect on the increase of surface energy by roughening surface area or formation of polar chemical bonds in the surface region. However in this research, since little changes of the surface roughness were detected between the 200 W and 900 W plasma power, it is hence concluded that the surface roughness plays a minor role in the enhancement of FCCL. From the park et al. surface energy was sharply increased when using N_2O gas compared to the pure Ar or O_2 gas because reactive species actively participated in forming new chemical bonding state like aromatic carbon bonded with N or O, and some parts improve the polar force [112]. Thus, in this aspect, I believe that the modification of chemical functional group caused by many N, Ar radicals generated in high plasma density probably increases the surface energy, and then leads to the enhancement of peel strength of the FCCL.

3.3 XPS analysis of the plasma treated FCCL films after peel test

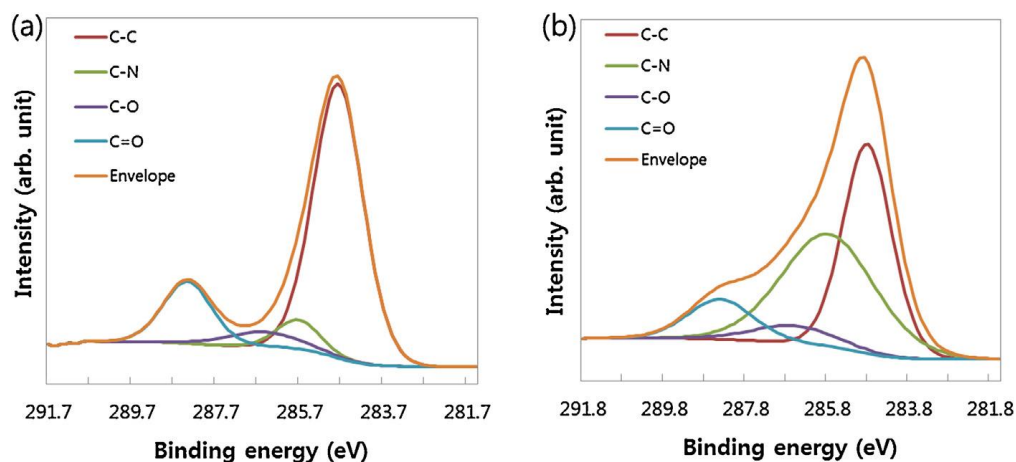


Figure 39 XPS C 1s spectra of the fractured PI surface for two samples: (a) 200 W and (b) 900 W.

Samples	Component ratio (%)			
Binding energy (eV)	284.7	285.8	286.6	288.6
Binding state	C—C	C—N	C—O	C=O
Plasma treatment (200 W)	72.5	7.8	7.2	12.5
Plasma treatment (900 W)	39.2	44.6	6.5	9.7

Table 1 XPS C 1s spectra of the plasma treated two FCCL: (a) 200 W, (b) 900 W.

Fig. 39 shows the C 1s core-level XPS spectrum of the peeled PI surface. The C 1s XPS spectra were deconvoluted into four different component peaks by Gaussian curve-fitting, and the peaks can be assigned to C-C (284.7 eV), C-N (285.6 eV), C-O (286.3 eV), and C=O (288.6 eV) bonds, respectively [104]. However, separation between the C-H bonds and C-C bonds was impossible due to their similar binding state.

I can observe from the table 1 that the component ratios of the PI surfaces treated at 200 W was completely different from that of the PI film treated at 900 W. Especially, noticeable changes of the C-C and C-N peaks were observed. The component ratio of the C-N bonding was drastically increased from 7.8 % to 44.6 % after 900 W plasma treatment, while C-C bonding significantly decreased from 72.5 % to 39.2 %. However, compared to the C-C, C-N bonding, the component ratios of the C-O and C=O bond were rarely changed by changing plasma power from the 200 W to 900W. Thus, this increase in the component ratio of the C-N bonding for the sample treated at 900 W is attributed to the substantial decrease in the component ratio of the C-C bonding. It is plausible that high plasma density generated at the power of 900W causes the significant increase of dissociated nitrogen radicals and, resulting in an substantial increase in the concentration of nitrogen atoms on the PI surface. To confirm the change of plasma characteristics indirectly, deposition rate of silicon nitride was measured in ICP CVD system as a function of RF power (as not shown here). It is found that the deposition rate of the silicon nitride increased with RF power. In the low power electrostatic regime, the film deposition rate is normally 2.7nm/min. However, varying the RF power from 200 W to 900 W, a significant increase from 2.9nm/min to 11.3nm/min in the deposition rate was obviously seen. Especially, noticeable change of growth rate was investigated in the power range of 200W - 500W, which means that capacitively coupled E mode transferred to the inductively coupled H mode in ICP discharge [94]. From these results of growth rate, I believed that high plasma density is the critical factor generating large C-N chemical functional groups on the PI surface. By changing the structure of the outer surface of the PI substrate with ICP plasma system, an increase in the number of nucleation site can be induced and it can act as a strong

coordinating ligand toward the metallic species, which is closely related with an interfacial bonding between the NiMoNb adhesion layer and PI surface. As mentioned before, a number of C-C bonds were broken in the high density plasma environment and these many broken bonds rearranged themselves to C-N bonds. Thus, strong C-N-metal complex could be formed between the NiMoNb and PI substrate, which enhances peel strength. Previous study also reported that the chemical functional groups such as hydroxyl, carbonyl and carboxyl are important species to promote peel strength between the PI and metals [84, 113]. Mittal et al. stated that the C-N and C-O chemical functionalities of polystyrenes increased after oxygen and nitrogen plasma, and hence yield a strong covalent linkage between the polystyrene and metals [114]. Furthermore, Kim et al. reported that the carbon atoms near the PI surface were rearranged and formed new structures, and a number of the C-O bonds increased after O₂ plasma treatment [84]. In addition, Jordan et al. found that Cr reacts with carbonyl oxygen atoms existed on the PI surface at the initial stage of growth [115], and also burkstrand et al. concluded that the chemical functional group such as C-O interacts with metals to form chelate-like complex, which improve peel strength [116]. The results of Fig. 4, 5 and table 1, enabled me to conclude that superior peel strength in this FCCL structure is tremendously dominated by the high C-N chemical functional groups caused by great plasma density in ICP plasma system. To observe any other phenomena on the degradation of peel strength after heat treatment, interfaces of the Cu/NiMoNb/PI were investigated in detail by HR-TEM.

3.4. TEM analysis

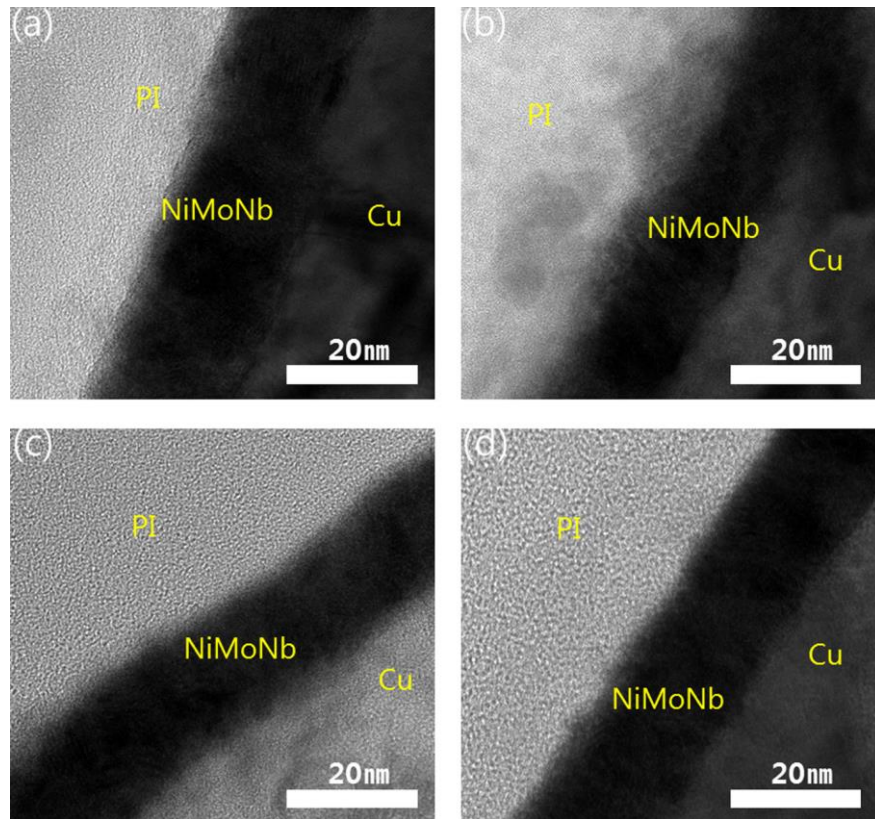


Figure 40 Cross-sectional HR-TEM image obtained from (a) 200 W plasma-pretreated FCCL samples, (b) 200 W plasma-pretreated FCCL samples subjected to annealing at 150°C for 24 h, (c) 900 W plasma-pretreated FCCL samples, (d) 900 W plasma-pretreated FCCL samples subjected to annealing at 150°C for 24 h.

We utilized HR-TEM to examine detailed observation on the NiMoNb/PI interfaces before and after heat treatment for the 200 W plasma-treated FCCL and 900 W plasma-treated FCCL as shown Fig. 40. In the case of as-deposited, little difference was observed in the interfacial roughness between the NiMoNb layer and PI substrate for both the 200 W plasma-treated FCCL and the 900 W plasma-treated FCCL, and this result is in good agreement with those obtained from AFM as shown in Fig 4. Therefore,

it can be concluded that plasma treatment have little effect on the roughness of the NiMoNb/PI interface in our system. However, compared to the as-deposited FCCL, considerable changes of the NiMoNb/PI interface were detected after heat treatment, only for the 200 W plasma-treated FCCL as shown Fig. 40(a) and 40(b). Some precipitates were observed in the PI substrate, providing the evidence of the diffusion of the metal inside the PI substrate, which is probably due to the weak and defective site of the metal/PI interface. Shih et al. suggested that thermal degradation of the peel strength is greatly accelerated when PI is contact with Cu [117]. In fact under this process condition, I confirmed that the peel strength of 411 N/m was obtained. However, 900 W plasma-treated FCCL showed no change of NiMoNb/PI interface after heat treatment. I believe that this difference is attributed to the degree of the chemical reaction at the NiMoNb/PI interface, and hence the higher C-N chemical functional group, the higher peel strength. It appears that the number of C-N chemical functional groups at the NiMoNb/PI interface plays a crucial role in stabilizing NiMoNb/PI interface even after heat treatment and reduces the degree of degradation in the peel strength by blocking diffusion of the metals inside of the PI substrate, which leads to high peel strength. According to the Iwamori et al. and AHN et al., the degradation of peel strength after heat treatment is attributed to the oxidation at the metal/PI interface [90, 118]. The major source of oxidation was proposed to be moisture contained either in polyimide or in air that diffused through polyimide to the interface. The changes in the peel before and after heat treatment were quantified in terms of a degradation factor (β), which is the ratio of the peel strength between the as-deposited and annealed FCCL samples. The degradation factor, β for the 200 W and 900 W plasma-treated FCCL was approximately 43 % and 12 %, respectively, which differs almost four times. Based on

the results of XPS and TEM, it can be concluded that the degradation in the peel strength after heat treatment is attributed to the collapsed state of NiMoNb/PI interfaces, which leads to the diffusion of metals such as Cu and Mo into the PI, and this was originated from the degree of the C-N chemical functional groups induced by the high plasma density in ICP system.

4. Conclusions

In this work, the effects of the sputtering power and pretreatment of PI using an internal type of ICP plasma on the peel strength of Cu/NiMoNb/PI system have been investigated. It was shown that the increase of the sputtering power improved peel strength, resulted from the increase of film density from 5.6 g/cm^3 to 9.7 g/cm^3 caused by effect of the ion bombardment. The results from the AFM and XPS showed that the surface roughness at two types of plasma condition was rarely changed, while the ratio of the C-N chemical functional group between 200 W and 900 W was tremendously changed from 7.8 % to 44.6 % due to the change of plasma characteristics. The peel strength of the as-deposited and annealed FCCL was 1050 N/m and 923 N/m, respectively obtained under the 900 W plasma treatment, which is the highest value compared to the previous researches. In addition, the degradation factor(β) of the peel strength was 43 % and 12 %, respectively for the 200 W and 900 W plasma-treated FCCL. For the 200 W plasma-treated FCCL, NiMoNb/PI interface was collapsed in some areas and metal diffused into the PI substrate after heat treatment. However, no change of the NiMoNb/PI interface and no metal diffusion were observed for the 900 W

plasma-treated FCCL. Therefore, a number of C-N chemical functional groups generated in high plasma density play a crucial role in enhancing peel strength, even after heat treatment by stabilizing NiMoNb/PI interface.

Reference

1. van de Weijer, P., et al., *High-performance thin-film encapsulation for organic light-emitting diodes*. Organic Electronics, 2017. **44**: p. 94-98.
2. Yun, S.-J., et al., *Water vapor transmission rate property of SiN_x thin films prepared by low temperature (<100 °C) linear plasma enhanced chemical vapor deposition*. Vacuum, 2018. **148**: p. 33-40.
3. Kim, E., et al., *Thin film encapsulation for organic light emitting diodes using a multi-barrier composed of MgO prepared by atomic layer deposition and hybrid materials*. Organic Electronics, 2013. **14**(7): p. 1737-1743.
4. Han, Y.C., et al., *The encapsulation of an organic light-emitting diode using organic-inorganic hybrid materials and MgO*. Organic Electronics, 2011. **12**(4): p. 609-613.
5. Lu, M.H., et al., *High-efficiency top-emitting organic light-emitting devices*. Applied Physics Letters, 2002. **81**(21): p. 3921.
6. Brabec, C.J., et al., *Origin of the Open Circuit Voltage of Plastic Solar Cells*. advanced functional material, 2001. **11**(5): p. 374-379.
7. Chen, T.N., et al., *High-Performance Transparent Barrier Films of SiO_x/SiN_x Stacks on Flexible Polymer Substrates*. Journal of The Electrochemical Society, 2006. **153**(10): p. F244.
8. Li, Y., et al., *Flexible top-emitting electroluminescent devices on polyethylene terephthalate substrates*. Applied Physics Letters, 2005. **86**(15): p. 153508.
9. Park, E.K., et al., *Electrical evaluation of crack generation in SiN_x and SiO_x N_y thin-film encapsulation layers for OLED displays*. Applied Surface Science, 2016. **370**: p. 126-130.
10. Do, L.-M., et al., *Morphological change in the degradation of Al electrode surfaces of electroluminescent devices by fluorescence microscopy and AFM*. Thin Solid Film 1996. **273**: p. 209-213.
11. Do, L.M., et al., *Observation of degradation processes of Al electrodes in organic electroluminescence devices by electroluminescence microscopy, atomic force microscopy, scanning electron microscopy, and Auger electron spectroscopy* Journal of Applied Physics, 1994. **76**: p. 5118-5123.
12. McElvain, J., et al., *Formation and growth of black spots in organic light-emitting diodes* Journal of Applied Physics, 1996. **80**: p. 6003-6009.
13. Aziz, H., et al., *Humidity-induced crystallization of tris (8-hydroxyquinoline) aluminum layers in organic light-emitting devices*. Applied Physics Letters, 1998. **72**(7): p. 756-760.
14. Gautier, E., et al., *Electrode interface effects on indium-tin-oxide polymer/metal light emitting diodes*. Applied Physics Letters, 1996. **69**: p. 1071-1076.
15. Schaer, M., et al., *Water Vapor and Oxygen Degradation Mechanisms in Organic*. ADVANCED FUNCTIONAL MATERIAL, 2001. **11**(2): p. 116-121.
16. Lau, K., et al., *Reactive pulse magnetron sputtered SiO_xN_y coatings on polymers*. Thin Solid Films, 2009. **517**(10): p. 3110-3114.

17. Jeong, J.-A. and H.-K. Kim, *Al₂O₃/Ag/Al₂O₃ multilayer thin film passivation prepared by plasma damage-free linear facing target sputtering for organic light emitting diodes*. *Thin Solid Films*, 2013. **547**: p. 63-67.
18. Kuo, C.-C., et al., *Improving the gas barrier property of SiO_x:C thin films deposited by RF magnetron sputtering*. *Surface and Coatings Technology*, 2015. **279**: p. 161-165.
19. Jin, S.B., et al., *Characterization of silicon oxide gas barrier films with controlling to the ion current density (ion flux) by plasma enhanced chemical vapor deposition*. *Thin Solid Films*, 2010. **518**(22): p. 6385-6389.
20. Nakayama, H. and M. Ito, *Super H₂O-barrier film using Cat-CVD (HWCVD)-grown SiCN for film-based electronics*. *Thin Solid Films*, 2011. **519**(14): p. 4483-4486.
21. Spee, D.A., J.K. Rath, and R.E.I. Schropp, *Using hot wire and initiated chemical vapor deposition for gas barrier thin film encapsulation*. *Thin Solid Films*, 2015. **575**: p. 67-71.
22. Carcia, P.F., et al., *Ca test of Al₂O₃ gas diffusion barriers grown by atomic layer deposition on polymers*. *Applied Physics Letters*, 2006. **89**(3): p. 031915.
23. Jeong, J.-A., et al., *Characteristics of Transparent SiN_[sub x] Thin-Film Passivation Layer Grown by CECVD for Top-Emitting OLEDs*. *Journal of The Electrochemical Society*, 2007. **154**(12): p. J402.
24. Heya, A., et al., *Effect of Atomic Hydrogen on Preparation of Highly Moisture-Resistive SiN_xFilms at Low Substrate Temperatures*. *Japanese Journal of Applied Physics*, 2004. **43**(No. 12A): p. L1546-L1548.
25. Spee, D., et al., *Excellent organic/inorganic transparent thin film moisture barrier entirely made by hot wire CVD at 100 °C*. *physica status solidi (RRL) - Rapid Research Letters*, 2012. **6**(4): p. 151-153.
26. Seo, S.-W., et al., *Optimization of Al₂O₃/ZrO₂ nanolaminate structure for thin-film encapsulation of OLEDs*. *Organic Electronics*, 2012. **13**(11): p. 2436-2441.
27. Yong-Qiang, Y., et al., *High barrier properties of transparent thin-film encapsulations for top emission organic light-emitting diodes*. *Organic Electronics*, 2014. **15**(6): p. 1120-1125.
28. Carcia, P.F., et al., *Gas diffusion ultrabarriers on polymer substrates using Al_[sub 2]O_[sub 3] atomic layer deposition and SiN plasma-enhanced chemical vapor deposition*. *Journal of Applied Physics*, 2009. **106**(2): p. 023533.
29. Tsai, Y.-S., et al., *Flexible fluorescent white organic light emitting diodes with ALD encapsulation*. *Journal of Physics and Chemistry of Solids*, 2015. **83**: p. 135-139.
30. Li, M., et al., *Facilitation of transparent gas barrier using SiN_x/a-IZO lamination for organic light emitting diodes*. *Organic Electronics*, 2015. **24**: p. 57-64.
31. Singh, A., et al., *OLED compatible water-based nanolaminate encapsulation systems using ozone based starting layer*. *Organic Electronics*, 2014. **15**(10): p. 2587-2592.
32. Burrows, P.E., et al., *Reliability and degradation of organic light emitting devices*. *Applied Physics Letters*, 1994. **65**(23): p. 2922-2924.
33. Lewis, J.S. and M.S. Weaver, *Thin-Film Permeation-Barrier Technology for Flexible Organic Light-Emitting Devices*. *IEEE Journal of Selected Topics in Quantum Electronics*, 2004. **10**(1): p. 45-57.

34. Weaver, M.S., et al., *Organic light-emitting devices with extended operating lifetimes on plastic substrates*. Applied Physics Letters, 2002. **81**(16): p. 2929-2931.
35. Yun, S.J., Y.-W. Ko, and J.W. Lim, *Passivation of organic light-emitting diodes with aluminum oxide thin films grown by plasma-enhanced atomic layer deposition*. Applied Physics Letters, 2004. **85**(21): p. 4896-4898.
36. <http://www.permeation-mocon.com/>.
37. Schubert, S., et al., *Electrical calcium test for moisture barrier evaluation for organic devices*. Rev Sci Instrum, 2011. **82**(9): p. 094101.
38. Park, J.-S., et al., *Thin film encapsulation for flexible AM-OLED: a review*. Semiconductor Science and Technology, 2011. **26**(3): p. 034001.
39. Dameron, A.A., et al., *Gas Diffusion Barriers on Polymers Using Multilayers Fabricated by Al₂O₃ and Rapid SiO₂ Atomic Layer Deposition*. J. Phys. Chem. C, 2008. **112**: p. 4573-4580.
40. Goldston, R.J. and P.H. Rutherford, *introduction to plasma physics*.
41. Lee, H.Y., et al., *Low temperature deposition of tin oxide films by inductively coupled plasma assisted chemical vapor deposition*. Thin Solid Films, 2008. **516**(11): p. 3538-3543.
42. Xu, S., et al., *Low-frequency, high-density, inductively coupled plasma sources: Operation and applications*. Physics of Plasmas, 2001. **8**(5): p. 2549-2557.
43. Hwang, N.M., J.H. Hahn, and D.Y. Yoon, *Charged cluster model in the low pressure synthesis of diamond*. Journal of Crystal Growth, 1996. **162**.
44. Jung, J.-S., et al., *Non-classical crystallization of silicon thin films during hot wire chemical vapor deposition*. Journal of Crystal Growth, 2017. **458**: p. 8-15.
45. Hwang, N.M., *Crystal growth by charged cluster focused on CVD diamond process*. Journal of Crystal Growth, 1999. **198-199**.
46. Sunagawa, I., *Growth and morphology of diamond crystals under stable and metastable conditions*. Journal of Crystal Growth, 1990. **99**(1-4).
47. Takamura, Y., et al., *High-rate deposition of YBa₂Cu₃O_{7-x} films by hot cluster epitaxy*. Journal of Applied Physics, 1998. **84**.
48. Ahn, H.-S., et al., *Observation of carbon clusters of a few nanometers in the oxyacetylene diamond CVD process*. Journal of Crystal Growth, 2002. **234**.
49. Jeon, i.-D., et al., *Temperature dependence of the deposition behavior of yttria stabilized zirconia CVD films Approach by charged cluster model*. Journal of THE Korean Ceramic Society 2001. **38**(3).
50. Adachi, M., et al., *Morphology control of films formed by atmospheric-pressure chemical vapor deposition using tetraethylorthosilicate/ozone system*. Jpn J. Appl. Phys, 1996. **35**.
51. Adachi, M., K. Okuyama, and N. Tohge, *Particle generation and film formation in an atmospheric-pressure chemical vapour deposition process using tetraethylorthosilicate*. Journal of Materials Science, 1995. **30**.
52. Monaghan, D.P., D.G.T.a.K.C. Laing, and I.E.a.R.D. Arnell, *Deposition of graded alloy nitride films by closed field unbalanced magnetron sputtering* Surface and Coatings Technology, 1993. **59**: p. 21-25.
53. Carcia, P.F., et al., *Ca test of Al₂O₃ gas diffusion barriers grown by atomic layer deposition on polymers*. Applied Physics Letters, 2006. **89**(3): p. 031915.
54. Hwang, N.M., *Non-Classical Crystallization of Thin Films and Nanostructures*

- in CVD and PVD Process*. Springer 2016. **60**.
55. Kusaka, I., Z.-G. Wang, and J.H. Seinfeld, *Ion induced nucleation A density functional approach*. J. Chem. Phys, 1994. **102**(2): p. 913-924.
 56. Wen, F.C., T. McLaughlin, and J.L. Katz, *Photoinduced nucleation of supersaturated vapors in the presence of carbon disulfide*. PHYSICAL REVIEW A, 1981. **26**(4): p. 2235-2242.
 57. Kersten, H., et al., *Complex (dusty) plasmas: Examples for applications and observation of magnetron-induced phenomena*. Pure and Applied Chemistry, 2005. **77**(2).
 58. Jung, J.-s. and N.-m. Hwang, *Non-Classical Crystallization of Thin Films and Nanostructures in CVD Process*. 2016.
 59. CLARE, B.W., et al., *Effect of Charge on Bond Strength in hydrogenated amorphous silicon_1996_journal of computational chemistry*. Journal of Computational Chemistry,, 1993. **15**(6): p. 644-652.
 60. Lin, T.-Y. and C.-T. Lee, *Organosilicon function of gas barrier films purely deposited by inductively coupled plasma chemical vapor deposition system*. Journal of Alloys and Compounds, 2012. **542**: p. 11-16.
 61. Fahlteich, J., et al., *Permeation barrier properties of thin oxide films on flexible polymer substrates*. Thin Solid Films, 2009. **517**(10): p. 3075-3080.
 62. Wu, D.S., et al., *Properties of SiO₂-like barrier layers on polyethersulfone substrates by low-temperature plasma-enhanced chemical vapor deposition*. Thin Solid Films, 2004. **468**(1-2): p. 105-108.
 63. Majee, S., et al., *The effect of argon plasma treatment on the permeation barrier properties of silicon nitride layers*. Surface and Coatings Technology, 2013. **235**: p. 361-366.
 64. Fahlteich, J., et al., *Characterization of reactively sputtered permeation barrier materials on polymer substrates*. Surface and Coatings Technology, 2011. **205**: p. S141-S144.
 65. Kim, H.-K. and C.-K. Cho, *Transparent SiON Ag SiON multilayer passivation grown on a flexible polyethersulfone substrate using a continuous roll to roll sputtering system_2012_nano express*. Nanoscale Research Letters, 2012. **7**: p. 69.
 66. Liu, K.-C., et al., *Investigation of SiO_xC_y film as the encapsulation layer for full transparent OLED using hollow cathode discharge plasma at room temperature*. Thin Solid Films, 2010. **518**(22): p. 6195-6198.
 67. Kaya, S., et al., *Samarium oxide thin films deposited by reactive sputtering: Effects of sputtering power and substrate temperature on microstructure, morphology and electrical properties*. Materials Science in Semiconductor Processing, 2015. **33**: p. 42-48.
 68. Lin, M.C., et al., *Characterization of the silicon oxide thin films deposited on polyethylene terephthalate substrates by radio frequency reactive magnetron sputtering*. Thin Solid Films, 2007. **515**(11): p. 4596-4602.
 69. Jeong, S.-H., et al., *Characterization of SiO₂ and TiO₂ films prepared using rf magnetron sputtering and their application to anti-reflection coating*. Vacuum, 2004. **76**(4): p. 507-515.
 70. LETERRIER, Y., et al., *Adhesion of silicon oxide layers on poly ethylene terephthalate I Effect of substrate properties on coating's fragmentation process_1997_Polym.Phys.* JOURNAL OF POLYMER SCIENCE PART B:

- POLYMER PHYSICS, 1997. **35**(9).
71. Zhang, L., et al., *Microstructure, residual stress, and fracture of sputtered TiN films*. Surface and Coatings Technology, 2013. **224**: p. 120-125.
 72. Prasanna Kumari, T., et al., *Effect of thickness on structure, microstructure, residual stress and soft magnetic properties of DC sputtered Fe₆₅Co₃₅ soft magnetic thin films*. Journal of Magnetism and Magnetic Materials, 2014. **365**: p. 93-99.
 73. Srinivas, K., et al., *Effect of sputtering pressure and power on composition, surface roughness, microstructure and magnetic properties of as-deposited Co₂FeSi thin films*. Thin Solid Films, 2014. **558**: p. 349-355.
 74. Zhang, S., et al., *Effect of sputtering target power density on topography and residual stress during growth of nanocomposite nc-TiN/a-SiN_x thin films*. Diamond and Related Materials, 2004. **13**(10): p. 1777-1784.
 75. Grüniger, A., et al., *Influence of film structure and composition on diffusion barrier performance of SiO_x thin films deposited by PECVD*. Surface and Coatings Technology, 2006. **200**(14-15): p. 4564-4571.
 76. Wen, F.C., T. McLaughlin, and J.L. Katz, *Photoinduced nucleation of supersaturated vapors in the presence of carbon disulfide*. PHYSICAL REVIEW A, 1982. **26**(4): p. 2236-2242.
 77. Jeong, J.-A., H.-K. Kim, and M.-S. Yi, *Effect of Ag interlayer on the optical and passivation properties of flexible and transparent Al₂O₃/Ag/Al₂O₃ multilayer*. Applied Physics Letters, 2008. **93**(3): p. 033301.
 78. Lewis, J.S. and M.S. Weaver, *<Thin-film permeation-barrier technology for flexible organic light emitting devices_2004_IEEE journal of selected topics in quantum electronics_.pdf>*. IEEE JOURNAL OF SELECTED TOPICS IN QUANTUM ELECTRONICS,, 2004. **10**(1): p. 45.
 79. Zhang, S., W. Xue, and Z. Yu, *Moisture barrier evaluation of SiO_x/SiN_x stacks on polyimide substrates using electrical calcium test*. Thin Solid Films, 2015. **580**: p. 101-105.
 80. Bang, S.-H., et al., *Application of NiMoNb adhesion layer on plasma-treated polyimide substrate for flexible electronic devices*. Thin Solid Films, 2014. **558**(2).
 81. Hwang, S.-M., et al., *Fabrication of two-layer flexible copper clad laminate by electroless-Cu plating on surface modified polyimide*. Transactions of Nonferrous Metals Society of China, 2009. **19**(4): p. 970-974.
 82. Noh, B.-I., et al., *Effect of thermal treatment on adhesion strength of Cu/Ni-Cr/polyimide flexible copper clad laminate fabricated by roll-to-roll process*. Microelectronic Engineering, 2011. **88**(5): p. 718-723.
 83. Noh, B.-I., J.-W. Yoon, and S.-B. Jung, *Effect of Ni-Cr seed layer thickness on the adhesion characteristics of flexible copper clad laminates fabricated using a roll-to-roll process*. Metals and Materials International, 2010. **16**(5): p. 779-784.
 84. Kim, S.H., et al., *Effect of surface roughness on the adhesion properties of Cu/Cr films on polyimide substrate treated by inductively coupled oxygen plasma*. Surface and Coatings Technology, 2005. **200**(7): p. 2072-2079.
 85. Ramos, M.M.D., *Theoretical study of metal polyimide interfacial properties*. Vacuum 2002. **64**: p. 255-260.
 86. Noh, B.-I., J.-W. Yoon, and S.-B. Jung, *Effect of laminating parameters on the adhesion property of flexible copper clad laminate with adhesive layer*.

- International Journal of Adhesion and Adhesives, 2010. **30**(1): p. 30-35.
87. Piqué, A., et al., *A novel laser transfer process for direct writing of electronic and sensor materials_1999_applied physics A*. Applied Physics A Materials Science & Processing, 1999. **69**: p. 279-284.
 88. Smith, A.T., et al., *Laser Direct Write Fabrication of Meta-Antennas for Electro Optic Conversion_2012_journal of laser micro nanoengineering*. JLMN-Journal of Laser Micro/Nanoengineering, 2012. **7**(3): p. 306-310.
 89. OLLINGER, M., et al., *Laser Direct-Write of Polymer Nanocomposites_2006_journal of laser micro nanoengineering*. JLMN-Journal of Laser Micro/Nanoengineering, 2006. **1**(2): p. 102-105.
 90. AHN, E.C., J. YU, and I.S. PARK, *Effect of heat treatment at 350 on the adhesion of CuCr alloy films to polyimide*. Journal of materials science, 2000. **35**: p. 1949-1955.
 91. Kondoh, E., *Material characterization of Cu Ti polyimide thin film stacks*. Thin Solid Films, 2000. **359**: p. 255-260.
 92. Yang, C.-h., et al., *The properties of copper films deposited on polyimide by nitrogen and oxygen plasma pre-treatment*. Applied Surface Science, 2005. **252**(5): p. 1818-1825.
 93. Park, S.C., S.S. Yoon, and J.D. Nam, *Surface characteristics and adhesive strengths of metal on O₂ ion beam treated polyimide substrate*. Thin Solid Films, 2008. **516**(10): p. 3028-3035.
 94. Noh, B.-I., et al., *Adhesion characteristics of Cu/Ni-Cr/polyimide flexible copper clad laminates according to Ni:Cr ratio and Cu electroplating layer thickness*. Journal of Materials Science: Materials in Electronics, 2008. **20**(9): p. 885-890.
 95. Eom, J.S. and S.H. Kim, *Plasma surface treatment of polyimide for adhesive Cu/80Ni20Cr/PI flexible copper clad laminate*. Thin Solid Films, 2008. **516**(14): p. 4530-4534.
 96. Miyamura, T. and J. Koike, *The effects of Cr oxidation and polyimide degradation on interface adhesion strength in Cu/Cr/polyimide flexible films*. Materials Science and Engineering: A, 2007. **445-446**: p. 620-624.
 97. Vladimirov, S.V. and K. Ostrikov, *Dynamic self-organization phenomena in complex ionized gas systems: new paradigms and technological aspects*. Physics Reports, 2004. **393**(3-6): p. 175-380.
 98. Nunomura, S., et al., *Fabrication of Nanoparticle Composite Porous Films Having Ultralow Dielectric Constant*. Japanese Journal of Applied Physics, 2005. **44**(No. 50): p. L1509-L1511.
 99. Bang, S.H., et al., *Application of NiMoNb adhesion layer on plasma-treated polyimide substrate for flexible electronic devices*. Thin Solid Films, 2014. **558**: p. 405-410.
 100. Iwamori, S., et al., *Effect of an interfacial layer on adhesion strength deterioration between a copper thin film and polyimide substrates*. Vacuum, 1998. **51**(4): p. 615-618.
 101. Ahna, H.-S., et al., *Observation of carbon clusters of a few nanometers in the oxyacetylene diamond CVD process*. Journal of Crystal Growth, 2002. **234**: p. 399-403.
 102. Ektessabi, A.M. and S. Hakamata, *XPS study of ion beam modified polyimide*

- films*. Thin Solid Films, 2000. **377**: p. 621-625.
103. Chang, G.S., et al., *Mechanism for interfacial adhesion strength of an ion beam mixed Cu/polyimide with a thin buffer layer*. Applied Physics Letters, 1999. **74**(4): p. 522-524.
 104. Hegemann, D., H. Brunner, and C. Oehr, *Plasma treatment of polymers for surface and adhesion improvement*. Nuclear Instruments and Methods in Physics Research Section B: Beam Interactions with Materials and Atoms, 2003. **208**: p. 281-286.
 105. Byun, T.J., et al., *Surface Modification of Polyimide for Improving Adhesion Strength by Inductively Coupled Plasma*. Japanese Journal of Applied Physics, 2009. **48**(8): p. 08HL01.
 106. Usami, K., T. Ishijima, and H. Toyoda, *Rapid plasma treatment of polyimide for improved adhesive and durable copper film deposition*. Thin Solid Films, 2012. **521**: p. 22-26.
 107. Miyauchi, K. and M. Yuasa, *A study of adhesive improvement of a Cr–Ni alloy layer on a polyimide surface by low pressure gas plasma modification*. Progress in Organic Coatings, 2013. **76**(11): p. 1536-1542.
 108. Naddaf, M., et al., *Surface interaction of polyimide with oxygen ECR plasma*. Nuclear Instruments and Methods in Physics Research Section B: Beam Interactions with Materials and Atoms, 2004. **222**(1-2): p. 135-144.
 109. Min, K.-J., et al., *Interfacial Adhesion Characteristics Between Electroless-Plated Ni and Polyimide Films Modified by Alkali Surface Pretreatment*. Journal of Electronic Materials, 2009. **38**(12): p. 2455-2460.
 110. Park, D.-H. and W.-K. Choi, *Low energy O₂⁺ and N₂O⁺ ion beam modification of polyimide for improving adhesive strength of Cu/PI in roll-to-roll process*. Thin Solid Films, 2009. **517**(14): p. 4222-4225.
 111. Noh, B.-I., et al., *Effects of different kinds of seed layers and heat treatment on adhesion characteristics of Cu/(Cr or Ni–Cr)/PI interfaces in flexible printed circuits*. Journal of Materials Science: Materials in Electronics, 2010. **22**(7): p. 790-796.
 112. Park, J.-Y., et al., *Chemical reaction of sputtered Cu film with PI modified by low energy reactive atomic beam*. Applied Surface Science, 2006. **252**(16): p. 5877-5891.
 113. Noh, B.-I., J.-W. Yoon, and S.-B. Jung, *Fabrication and adhesion strength of Cu Ni Cr polyimide films for flexible printed circuits.pdf*. Microelectronic Engineering, 2011. **88**: p. 1024-1027.
 114. Mittal, K.L. and A. Pizzi, *Adhesion Promotion Techniques: Technical Applications*, ed. M. Dekker. 2002, New York.
 115. Jordan, J.L., *Synchrotron-radiation excited carbon 1s photoemission study of Cr/organic polymer interfaces*. Journal of Vacuum Science & Technology A: Vacuum, Surfaces, and Films, 1986. **4**(3): p. 1046.
 116. Burkstrand, J.M., *Formation of metal–oxygen–polymer complexes on polystyrene with nickel and chromium*. Journal of Vacuum Science and Technology, 1979. **16**(4): p. 1072-1074.
 117. Shih, D.-Y., *Oxygen induced adhesion degradation at metal/polyimide interface*. Journal of Vacuum Science & Technology A: Vacuum, Surfaces, and Films, 1991. **9**(6): p. 2963.
 118. Iwamori, S., et al., *Effect of an interfacial layer on adhesion strength*

deterioration between a copper thin film and polyimide substrates_1998_vacuum_, 1998. **51**(4): p. 615-618.

국문초록

플렉서블 유기발광 다이오드 디스플레이 경우 기존 액정 디스플레이 대비하여 색재현력, 명함비, 시야각, 소비전력 등의 특성이 우수하기 때문에 최근 디스플레이 시장에서 큰 관심을 받고 있으며 특히 BLU (Back Light Unit) 통해 빛을 내는 액정 디스플레이와 달리 유기 발광 다이오드 디스플레이의 경우 자체 발광하기 때문에 얇은 두께의 소자를 제작할 수 있어 디자인 설계 자유도 측면에서 매우 큰 장점이 있다. 이러한 우수한 특성을 가지고 있음에도 불구하고 플렉서블 유기 발광 다이오드 디스플레이의 경우 소자 제작 시 기판으로 폴리머 기판을 사용하기 때문에 기존 유리를 사용하던 액정디스플레이와 달리 대기중의 산소나 수분이 기판 안으로 잘 투과되어 유기재료 및 알루미늄 전극등과 반응하여 산화, 결정화, 박리 등의 문제를 야기시키며 결국 빛을 내지 않은 영역인 흑점을 발생시킨다. 따라서 이러한 문제를 해결하기 위해 외부로부터 수분을 차단할 수 있는 봉지막 기술이 크게 중요해지고 있다. 특히 최근 폴더블 디스플레이와 같이 곡률 반경 1.5mm 이하의 디스플레이에서는 얇으면서도 수분 투과 저항 특성이 우수한 박막 봉지 기술 개발이 매우 중요해지고 있다. 박막 봉지 기술은 폴리머 기판과 같은 유연 기판에 수분투과 방지막을 증착 하는 기술을 의미하며 기존 금속 캔/유리 봉지 방식에 비해 얇고, 가벼운 소자를 제작할 수 있는 장점을 가지고 있다. 그러나 박막 봉지 기술의 경우 박막의 두께가 얇고 증착 시 생기는 결함 등에 의해 수분 투과 특성이 기존 유리에 비해 특성이 떨어지는 단점이 있다. 이를 극복하기 위해 ViTEX 社에서 유기/무기 하이브리드 구조를 제안하였으며 이 구조는 수분 투과를 막아주는 고밀도의 무기막과 유연성을 확보 할 수 있는 유기막을 교대로 적층하여 공정 중 불순물 등으로 형성되는 무기막의 결함을 다층막 구조로 보완하고 유기층으로 봉지막의 유연성을 확보할 수 있게 하였다. 현재 세계적인 플렉서블 유기발광 다이오드 디스플레이 제조사들은 위에서 언급한 유기/무기막을 교대로 적층하여 수분 투과 방지막에 적용하고 있다. 다만 각 기업마다 유기/무기막 종류 및 최적화된 구조는 다르며 수분 투과 방지 특성이 뛰어나고 생산성이 우수한 방향으로의 물질 및 증착 기술에 대한 연구가 활발히 이루어지고 있다. 무기박막 봉지 기술의 경우 화학 기상 증착법 (Chemical Vapor Deposition), 원자층 증착법 (Atomic Layer Deposition), 스퍼터링 기법 (Sputtering)등을 통해 증착을 할 수 있는데, 이 기술들 중 원자층 증착법을 이용한 무기막 증착이 수분 투과 방지 특성에 있어 가장 우수하나 증착속도가 6-7nm/min 로 매우 낮아 양산기술에 적용하기까지는 아직 어려운 상황이다. 따라서 현재 기업에서는 무기막 증착의 경우 기상화학 증착법을 이용한 봉지막 기술 연구가 가장 많이 이루어 지고 있다. 그러나 기상화학 증착법의 경우도 봉지막 증착 시 공정온도가 100℃

이하에서 증착 되어야 하기 때문에 저온에서 결합이 적으면서도, 박막 밀도가 높은 고품질의 봉지막 형성이 쉽지 않으며 다양한 증착장비 및 공법 개발을 통해 낮은 온도에서 증착속도가 높으면서 수분투과 방지 특성이 우수한 박막 봉지 기술에 대한 연구가 활발히 진행 중이다.

본 연구의 첫 번째 주제는, 유도 결합 플라즈마를 활용한 플라즈마 기상화학 장치를 이용하여 수분 투과 방지 특성이 우수한 SiO_xNy 박막 개발 및 고품질의 수분투과 방지막 형성 원리를 하전된 나노입자 이론 기반인 비 고전적 박막 성장이론에 기반하여 박막 형성에 대한 새로운 통찰력을 제시하고자 하였다. 다양한 공정변수에 따라 기상에서 SiO_xNy 나노 입자가 생성되는 여부를 확인하기 위해 기상 나노 입자를 TEM (Transmission Electron Microscope) 그리드를 활용하여 포집 하였고, 포집된 입자를 투과전자 현미경으로 분석을 진행한 결과 20nm - 300nm 크기의 다양한 SiO_xNy 나노 입자가 기상에서 형성됨을 처음으로 확인 하는데 성공하였다. 이렇게 관찰된 나노 입자의 경우 공정 조건에 따라 나노 입자의 크기, 모양, 나노 입자간 응집 정도가 크게 다르게 확인 되었는데 특히 아르곤/실란 비율이 낮고, 파워가 낮을 경우 형성된 나노 입자의 크기가 크고, 모양이 불규칙적이며, 나노 입자들간의 응집이 크게 일어남을 확인 하였고 또한 비결정성 나노 입자임을 투과 전자현미경을 통해 확인하였다. 반면 아르곤/실란 비율이 높고 파워가 높을 수록 나노 입자의 크기가 작아지다가 일정 크기로 유지되면서, 원형의 나노입자가 생성 및 나노 입자들간 응집이 점점 없어졌다. 최적 조건에서는 나노입자들간의 응집현상이 전혀 없는 20-30nm 크기의 단일 원형 나노입자 확인 되었으며 특정 파워 조건에서는 균일한 크기의 단결정 나노 입자가 확인 되기도 하였다.

투과전자현미경을 통해 기상에서 생성된 초기 나노입자 거동을 확인 후 박막 증착을 통해 실제 수분 투과 저항 특성을 확인한 결과 아르곤/실란비율이 높고, 높은 파워에서 증착 된 박막이 아르곤 /실란 비율이 낮고, 낮은 파워에서 증착 된 박막대비 수분투과 저항특성이 1000 배 이상 차이 남을 확인하였다.

본 연구를 통해 초기 SiO_xNy 나노입자의 거동과 고밀도의 봉지막 형성과 큰 연관성이 있음을 처음으로 확인 하였고 저온에서 고밀도의 박막을 형성 할 수 있음을 비고전적 박막 성장이론을 바탕으로 처음으로 제시하였다.

이러한 비고전적 기상 화학 박막 성장이론 기반한 박막 물성 제어 연구는 향후 다양한 분야의 신규박막 및 물성제어 개발에 큰 역할을 할 것으로 기대한다.

본 연구의 두 번째 주제는 롤투롤 스퍼터링 시스템을 이용한 SiO_x 봉지막 필름에 관한 연구이다. 실리콘 산화물 (SiO_x) 배리어 필름을 마그네트론 스퍼터링 시스템을 사용하여 20 °C에서 PET 기판에 증착 시켰다. 최적의 SiO_x 배리어 막 개발을 위해 산소 유량, 스퍼터링 파워 및 막 두께를 제어 하였다. 스퍼터링 파워

및 막 두께 효과 확인을 위해 잔류 응력, 표면, 거칠기, 밀도, SiO_x / PET 의 계면 및 수분 투과 저항 특성에 대해서 분석 하였고 특히, 스퍼터링 파워가 최종 배리어 특성에 미치는 영향에 주목 하였다. 최적화된 배리어 필름의 경우 92 %의 높은 광 투과율을 보였고 2.42 g/cm³ SiO_x 고밀도를 가지는 필름을 확보하였다. 20 °C의 낮은 기판 온도에서도, 300 nm 두께의 SiO_x 배리어 필름은 7.7 × 10⁻³g /m²/day 의 우수한 WVTR 값을 나타냈다. 이러한 실험적 관찰은 SiO_x 막의 배리어 특성이 표면 거칠기, 계면 상태, 밀도 등 박막의 다양한 물성에 크게 영향을 받음을 확인 하였다.

주요어: 플렉서블 유기발광 다이오드 디스플레이, 봉지막, 유도 플라즈마 기상화학증착, 비고전적 기상 박막 성장, 하전된 나노입자 이론, 투과전자 현미경,

학 번 : 2013-30937

이 름 : 방 성 환